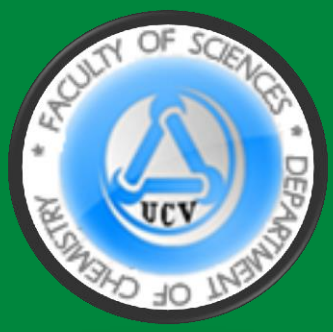

Annals of the University of Craiova
The Chemistry Series

Analele Universităţii din Craiova
Seria Chimie

Volume XLV, no. 1

2018

Contact
Phone: +40 251 597048
Fax: +40 251 597048
Web page: http://chimie.ucv.ro/departament/
e-mail: office@chimie.ucv.ro

Content

Annals of the University of Craiova
The Chemistry Series
Volume XLV, No. 1 (2018) 3-9
homepage: chimie.ucv.ro/anale/

Interaction of collagen with an azo dye

Research article

Anca Moanță[1,*], *Alberto Ristache*[2]

[1] University of Craiova, Faculty of Sciences, Department of Chemistry, Calea Bucuresti, 107i, Craiova, Romania
[2] Carol I College, Ion Maiorescu Street no. 2, Craiova, Romania
* E-mail: moantaanca@yahoo.com

Received: 19.01.2018 / Accepted: 21.02.2018 / Published: 16.07.2018

Abstract
Azo dye interact with proteins and form complexes. In this paper we studied the effect of the Methyl Red on collagen from skin by FTIR spectroscopy.

Keywords: azo dye, collagen, methyl red

1. INTRODUCTION

Dyes belong to a series of colored substances which have a great affinity to a substrate to which they are applied. They have a wide variety of applications: textile industry, paintings, cosmetics, food industry and chromophores in non-linear optics and inhibitors of carbon-steel corrosion [1, 2]. Many azoethers have been studied and showed antimicrobial activity [3].

Azoic dyes are the most common and the most important ones. So they are organic molecules which have the general formula: R-N=N-R', in which R, R' are organic radicals. They are prepared in laboratory

by azo coupling. This reaction implies 2 active components which represent the reactants. One of them is represented by a compound which is inclined to undergo an electrophilic substitution. In most cases it has the general formula: Ar-Z, where Z is a electron donating group (e.g. Z = -OH, $-NR_2$) while the other component is an aryl diazonium cation with the general formula $Y\text{-}Ar\text{-}N_2^{+,}$ where, in most cases, Y is an electron withdrawing group (e.g.: Y= $-NO_2$, -COOH, $CONR_2$).

In the latest years there has been a great debate regarding de issue of the probably harmful effects of using azo dyes in coloring toys, food or clothes because of the possibility that carcinogenic compounds may be formed when processed. One of the problems which were observed consists of the predisposition of dyes to form chelatic compounds with the proteins they get in contact with. The proteins chosen to be analyzed are BSA (bovine serum albumin) and collagen. Previous research show the fact that some dyes, like Brown HT and Tartrazine do form this kind of chelatic compounds with the proteins mentioned above. The interaction of these two dyes with BSA was studied using the UV-Vis spectrophotometry technique, attempting to prove the formation of chelatic complexes BSA-Tartrazine and BSA-Brown HT by analyzing the modification which appears in the UV-Vis electronic spectrum of dyes in the presence of variable quantities of BSA. FTIR spectroscopy technique was used to prove the structural modifications in the secondary structure of proteins when they interact with dyes. For this experiment it was chosen collagen for the interaction with Brown HT and Tartrazine. For analysis, it were mostly used the amide band I and the amide band II due to their sensitivity to structural changes of the molecule, especially amide band I which is significantly more sensitive that amide band II.

The compound Methyl Red, scientifically named (2-(N,N-dimethyl-4-aminophenyl)azobenzenecarboxylic acid is an azo dye which is red in acidic medium (pH<4.2), yellow at pH>6.2 and orange in between. In microbiology is used to identify bacteria which produce acids in formation processes of glucose.

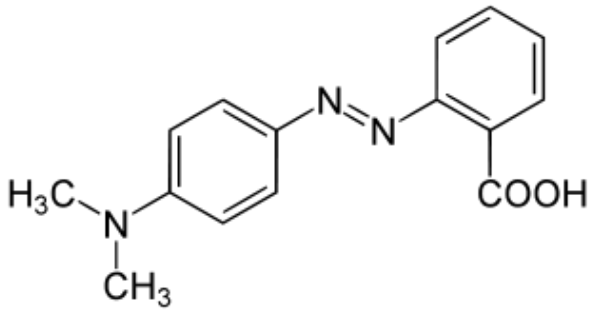

Scheme 1.Structure of Methyl Red

2. MATERIALS AND METHODS

2.1. Materials

Methyl Red and formic acid were purchase from Merck.

2.2. Method

For the painting of skin samples se it has been used an installation made of a magnetic stirrer equipped with a heating stove, contact thermometer and a test tube. 2 mL aqueous solution of dye at concentration of 10 % and 0.2 g of skin were put in a plastic tube and stirred magnetically for an hour at 20 °C. The dyeing bath was heated at 55 °C, 0.4 mL of water and 4mg of formic acid were added. The sample was stirred for 30 minutes and then rinsed with 4mL of water and dried at room temperature. [6]

FT-IR spectra were recorded on a Bruker ATR ZnSe spectrophotometer, within the range of 4000-550 cm^{-1}, at room temperature with a spectral resolution of 2 cm^{-1}.

3. RESULTS AND DISCUSSION

Skin made of structural proteins (88% collagen, 6% keratin, 0.9% elastin) and non-structural proteins (3% albumins and globulins, 2.1% mucins and mucoids).

Collagen is the most abundant protein in skin and, as a consequence, it can be assumed that FTIR spectrums of skin mainly depend on collagen absorptions. FTIR spectrum analysis of proteins indicate two important bands, named band amide I and band amide II. Band amide I is the most sensitive and is present in the region 1700-1600 cm-1 [7]. It was assigned to the vibrations of the bond strething for carbonyl group from the protein structure. Band amide II is present in the region 1650-1550 cm-1 and it was assigned to the vibrations of the stretching C-N and to the vibrations of bond bending of N-H.

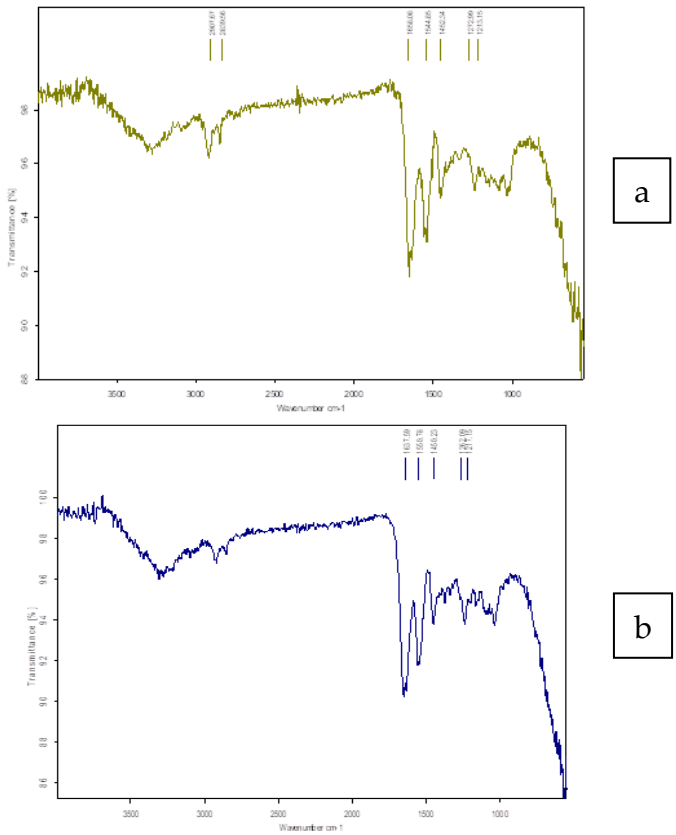

Figure 1. FTIR spectra of untreated skin samples (a spectrum) and treated skin samples with Methyl Red aqueous solution at a concentration of 10% (b spectrum)

In the FTIR spectrum of skin which was treated with solution of methyl red dye 10% band amide 1 is present at 1658 cm^{-1} and band amide II at 1550cm^{-1} (Figure 1).

In the FTIR spectrum of skin which was treated with solution of methyl red dye 10 % band amide 1 is present at 1658 cm^{-1} and band amide II at 1550cm^{-1} (Figure 1).

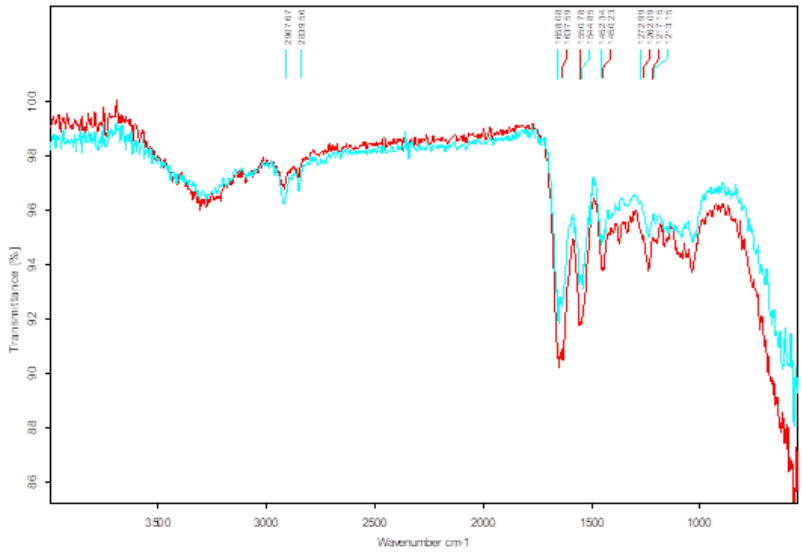

Figure 2. FTIR spectra of untreated skin sample (blue line) and treated with Methyl Red aqueous solution at a concentration of 10% (red line)

As it can be observed no modifications appear when it comes to the regions where bands amide I and amide II are present both for treated skin samples with solution of methyl red 10% and for untreated ones (Figure 2).

A thorough investigation of specific absorption bands is fundamental for gathering useful information about the interaction of dyes with skin proteins. Especially, FTIR spectroscopy technique was used massively for the study of collagen reticulation in bones and cartilage samples, by analyzing signal/noise ratio (S/N) in the region 1654-1690 cm^{-1}, ratio which grows proportionally with collagen reticulation. S/N can be calculated using two methods: peak to peak (PP) and root mean square (RMS).

Table 1. S/N ratio (1654/1690cm^{-1}) of the FTIR spectres of both treated with Methyl Red and untreated skin samples

Sample	Signal noise/ratio	
	RMS	PP
Untreated	434,376	144,949
Treated with Methyl Red aqueous solution at a concentration of 10 %	479,578	156,385

As can be seen from Table 1 and Figure 3, the S/N ratio increases for the treated skin sample compared to the untreated sample. Decrease in the S/N ratio is related to modification in enzymatic bond [8]. In this case, the S/N ratio modification is due to the interaction with the azo dye. This proves to form a complex between collagen and methyl red.

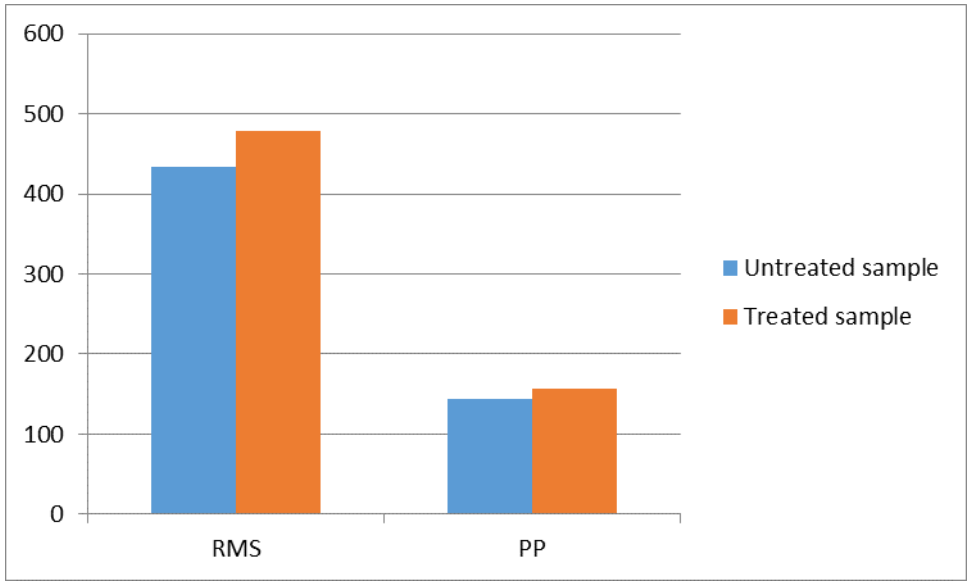

Figure 3. S/N ratio (1654/1690cm^{-1}) of the FTIR spectres of both untreated and treated skin samples with Methyl Red

4. CONCLUSION

The study of the interaction between Methyl Red dye and collagen from a skin sample using the FTIR spectroscopy technique highlighted the modification of absorption bands in the region 1654-1690 cm^{-1}. Absorption bands assigned to the vibration of C=0 bond are present at the same frequenices in the both cases when skin was treated with dye or when skin remained untreated. For the study of collagen reticulation we analyzed the S/N ratio in the region 1654-1690cm^{-1} and we observed larger values for the skin sample treated with azo dye than we did for the untreated skin sample due to the significantly structural changes of collagen caused by the interaction with dye. This modification proves the formation of a complex between azo dye and protein.

References

[1] S. Radu, C. Şarpe-Tudoran, A. Jianu and G. Rău, *Rev. Roum. Chim.*, 43 (1998) 735.

[2] A. Moanţă, B. Tutunaru and P. Rotaru, *J. Therm. Anal. Calorim.*, 111 (2013) 1273.

[3] A. Moanta, C. Ionescu and S. Iordache, *Ann. Univ. Craiova, Chemistry Series*, 2 (2017) 24.

[4] M. Leulescu, I. Pălărie, A. Moanţă, N. Cioateră, M. Popescu, E Morîntale, M. C. Văruț and P. Rotaru, *J. Therm. Anal. Calorim.*, 2018, online first, doi.org/10.1007/s10973-018-7766-x

[5] M. Leulescu, A. Rotaru, I. Pălărie, A. Moanţă, N. Cioateră, M. Popescu, E. Morîntale, M. V. Bubulică, G. Florian, A. Hărăbor and P. Rotaru, *J. Therm. Anal. Calorim.*, 134 (2018) 209.

[6] D. Pellegrini, M. Corsi, M. Bonanni, R. Bianchini, A. D'Ulivo and E. Bramanti, *Dyes Pigm.*, 116 (2015) 65.

[7] Q. Wang, W. Sanad, L. M. Miller, A. Voigt, K. Klingel, R. Kandolf R, *Vib Spectrosc*, 38 (2005) 217.

[8] H. D. Barth, E. A. Zimmermann, E. Schaible, S. Y.Tang, T. Alliston, R. O. Ritchie, *Biomaterials*, 32 2011 8892.

Annals of the University of Craiova
The Chemistry Series
Volume XLV, No. 1 (2018) 10-17
homepage: chimie.ucv.ro/anale/

Electrochemical and thermal behavior of 5-fluorouracil antitumor drug

Research article

*Cristian Neamțu, Bogdan Tutunaru**

University of Craiova, Faculty of Sciences, Department of Chemistry, Calea București 107i, Craiova, Romania
* E-mail: tutunaruchim@yahoo.com

Received: 22.01.2018 / Accepted: 28.02.2018 / Published: 16.07.2018

Abstract
Electrochemical interaction of 5-fluorouracil antitumor drug with titanium electrode surface was investigated by cyclic voltammetry in physiological serum as supporting electrolyte. UV-Vis spectrophotometry performed before and after cyclic voltammograms registration revealed that 5-fluorouracil drug is electrochemical active. The mechanism of electrochemical degradation is also proposed. Thermal stability of aqueous solution of 5-fluorouracil was studied by simultaneous TG-DSC thermal analysis. The experimental results show a step-by-step degradation process at temperatures higher than ~100 °C.

Keywords: 5-fluorouracil, electrochemistry, spectrophotometry, thermochemistry

1. INTRODUCTION

5-Fluorouracil (5FU) is a pyrimidine drug discovered by Heidelberger et al. [1] and designed as an antitumor drug. 5FU is marketed as injectable solution or creams for local applications to treats

a numerous types of solid tumors of pancreas, breast, neck, skin, head and colon [2-7]. 5-Fluorouracil and 5-fluorodeoxyuridine metabolite are responsible for the induction of apoptosis [2] by inhibition of thymidylate synthase activity and by direct incorporation into DNA and RNA strands.

Alternative methods of synthesis and characterization of 5-fluorouracil have been used in order to improve its antitumor activity [3, 4]. The existence of hydrogen bonds interactions of 5-fluorouracil have been investigated by mathematical modeling and density functional theory (DFT) [5-9].

Nanomaterials such as boron nitride nanotubes have been studied for 5FU adsorbent and enhanced system delivery [10]. New forms of 5FU with some dendrimers and anthelmintic piperazine have been studied as nano-transporters with delivering improved properties [11, 12]. Au-5FU and 5FU-chitosan nanoparticles have been successfully prepared in order to enhance its antitumos effect [13, 14].

This type of drugs have carcinogenic, mutagenic and genotoxic effects and cannot be eliminated by conventional treatments. Photodegradation of 5FU was studied by UV-Vis spectroscopy, High Performance Liquid Chromatography and High Resolution Mass Spectrometry [15-26].

The present study aims to determine the electrochemical behavior of 5-fluorouracil in aqueous solution in conditions similar to those for clinical use and to investigate the thermal behavior of 5FU as injectable solution.

2. MATERIALS AND METHODS

2.1. Materials

5-Fluorouracil (Sandoz) was purchased from a local pharmacy as 20 mL vials with a concentration of 50 $mg \cdot mL^{-1}$. Natrium chloride (Sigma-Aldrich) was of reagent grade and a stock solution of 0.9 % concentration was prepared and used. Titanium plates electrodes with an effective surface of 2 cm^2.

2.2. Analysis methods

Electrochemical analysis (Cyclic Voltammetry) was performed by a VoltaLab 40 using a three electrode one compartment electrochemical cell. Both anode and cathode were identical and represented by titanium plates (1x1 cm). A silver chloride electrode (KCl saturated) was used as reference electrode. VoltaMaster 4 software was used for control, data aquisition and data processing. Cyclic voltammograms were recorded with a potential sweep rate of 100 $mV \cdot sec^{-1}$ between -2.0 V and +2.0 V vs. reference electrode.

UV-Vis spectrophotometry of 0.9 % NaCl solution without and with 10^{-4} $mol \cdot L^{-1}$ 5FU, before and after cyclic voltammetry recording was performed using a Varian Cary UV-Vis spectrophotometer. UV-Vis spectra were recorded in a quartz spectrophotometric cell at room temperature.

Thermal analysis of 10^{-2} $mol \cdot L^{-1}$ 5FU was performed from room temperature to 500 °C. Experimental data were acquired with a heating rate of 5 $°C \cdot min^{-1}$ in an aluminium crucible. Both reference and working crucibles were made from aluminium. Thermal analysis was studied by a Perkin Elmer thermal analyser (Pyris software) in inert nitrogen atmosphere. The nitrogen gas was purged through the oven at a constant flow of 0.150 $L \cdot min^{-1}$.

3. RESULTS AND DISCUSSION

3.1. Electrochemical behavior of 5FU on Ti electrode

In Figure 1 are presented the cyclic voltamograms of titanium electrode in 0.9 % NaCl solution both in the absence and in the presence of 10^{-4} $mol \cdot L^{-1}$ 5FU.

As the potential of the working electrode is sweeped in the positive direction, it is observed that some peaks of current densities are recorded. This is observed both in the absence and presence of 5FU molecules and is most likely attributed to passive film formation on the

surface of the electrode. At potential values greater than -0.4 V, there is a slow increase in current densities, while at potentials values greater than 1.4 V the current densities are suddenly increased, this process is associated with passive layer breakdown and the beginning of the transpassive region (Figure 1).

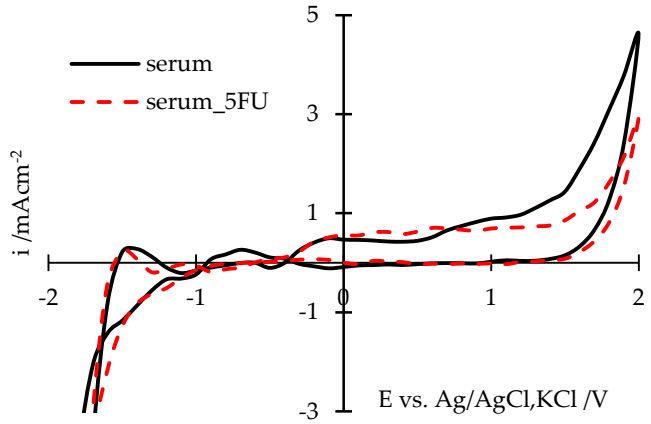

Figure 1. Cyclic voltammograms of Ti electrode in 0.9 % NaCl solution, in the absence and in the presence of 5FU 10^{-4} mol·L^{-1}, 100 mV·s^{-1}

When 5FU molecules are introduced into the electrolyte solution, there is also a change in the characteristics of the cyclic voltammogram. Thus, the current densities are lower than those recorded in the physiological serum, and the corresponding passivity range is wider with approximately 0.2 V. Knowing the electrocatalytic properties of titanium, this demonstrates the participation of 5FU molecules in electrode processes. This is also demonstrated by recording the UV-Vis spectra of the electrolyte solution before and after performing the cyclic voltammetry (Figure 2).

UV-Vis spectrophotometry analysis shows an absorbance peak in the UV domain (λ = 268 nm) characteristic to 5-fluororacil molecule (10^{-4} mol·L^{-1}) (Figure 2).

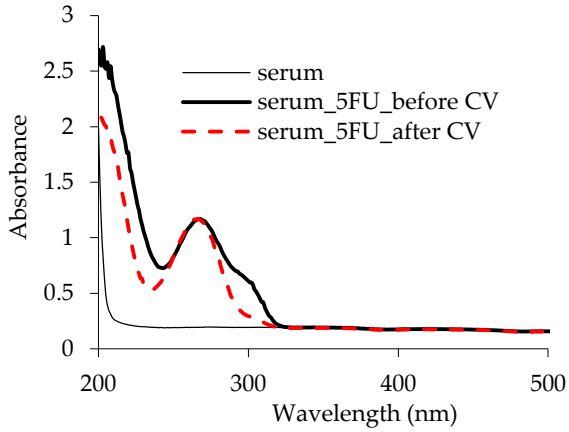

Figure 2. UV-Vis spectra of 0.9 % NaCl solution (fisiological serum) without and with 10^{-4} mol·L^{-1} 5FU, before and after cyclic voltammetry

The UV-Vis spectrum, recorded under the given experimental conditions, for the initially 5FU solution also has a low intensity (shoulder; λ = 300 nm) peak due to the co-presence in the tautomeric forms in the electrolyte solution (Scheme 1). The 5FU molecules participate in electrode processes, so the composition of the electrolyte solution changes and, implicitly, its UV-Vis spectrum. The maximum recorded at wavelength of 300 nm disappears completely, and absorbance values have higher values at wavelengths less than 250 nm.

Scheme 1. The structures of 5FU tautomers

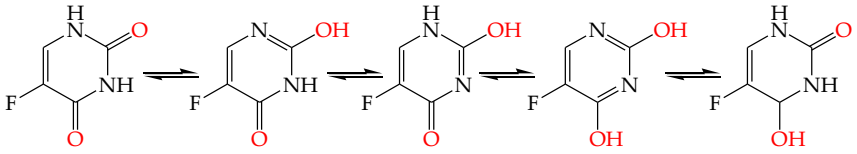

The results obtained by spectrophotometric analysis are consistent with those obtained by cyclic voltammetry and indicate the electrochemical degradation of 5FU molecules.

A proposed mechanism for electrochemical degradation of 5FU molecules is shown in Scheme 2.

Scheme 2. The mechanism of 5FU electrochemical degradation

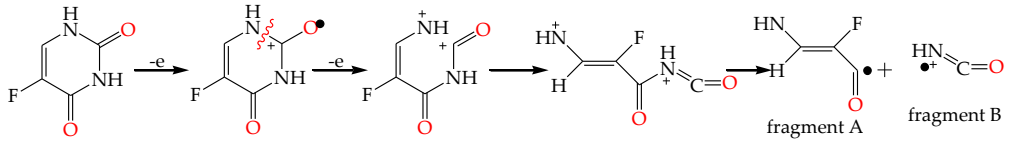

5FU molecules participate at the surface of the titanium electrode at deelectronation, tautomerization and ring opening processes with the formation of two fragments (A and B), as shown in Scheme 2.

Scheme 3. The mechanism of fragments A and B electrochemical degradation

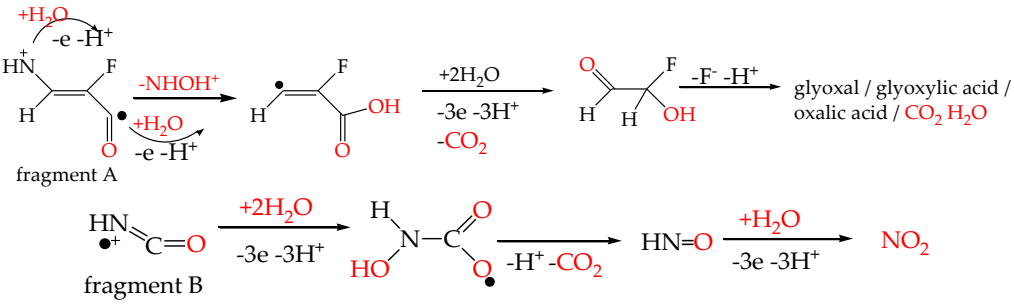

The A and B fragments are further oxidized to the surface of the electrode, so the nitrogen atoms are removed as hydroxylamine or nitrogen dioxide, while the fluorine atom is removed by defluorination (Scheme 3).

3.2. Thermal behavior of 5FU

The results of the thermal analysis presented as thermogravimetric curves (TG) and differential scanning calorimetry (DSC) of the 5FU injectable solution are shown in Figure 3.

According to Figure 3, it is observed that at temperatures lower than 95 degrees Celsius there is a sudden decrease in mass associated with water evaporation. The mass loss associated with the temperature range between ambient and 95 °C is 91.9 %. The thermal degradation of

fluorouracil molecules begins at a temperature of 150 °C as indicated by the detail of the TG curve (Figure 3).

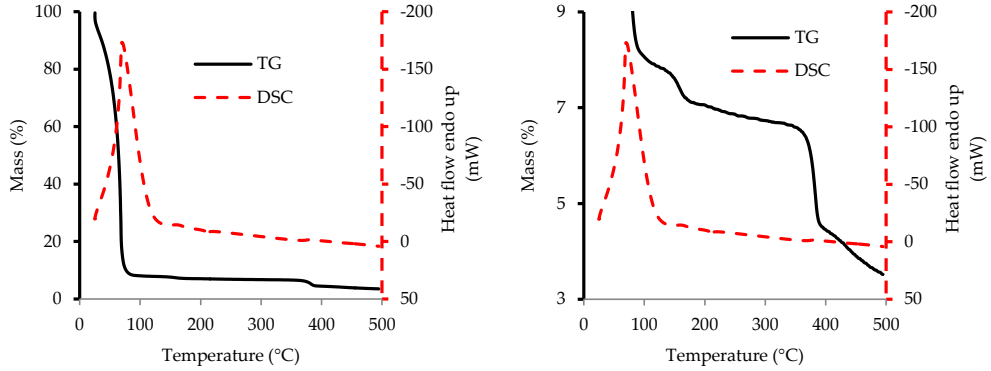

Figure 3. The TG/dTG and DSC/dDSC thermograms of 5FU injectable solution, heating rate 10 °C·min^{-1}

Thermal degradation of 5FU takes place in several successive steps as follows: in the temperature range 95 ÷ 170 °C, a mass loss of about 0.9 % is observed; in the temperature range 170 ÷ 351 °C, a mass loss of about 0.5 % is observed; in the temperature range 351 ÷ 388 °C, a higher mass loss of 2.2 % is registered; after the last stage of thermal degradation, between the temperatures 388 and 500 there is a decrease of the mass by 1 % and at the end of the experiment, in the crucible remains a 3.5 % residue.

4. CONCLUSION

Cyclic voltammetry of the 5FU antitumor drug shows that organic molecules are electrochemically active leading to a change in the shape of the cyclic voltammogram.

Spectrophotometric analysis of the electrolyte solution after cyclic voltammetry indicates the modification of the absorption maxima, demonstrating that the 5FU molecules are electrochemically degraded.

From the thermal analysis, the interpretation of the TG / DSC thermograms shows that 5FU compound is degraded on successive temperature ranges.

References

[1] R. Legay, S. Massou, J. Azéma, R. Martino, M. Malet-Martino, J. Pharm. Biomed. Anal., 98 (2014) 446.
[2] X. C. Li, K. G. Liu, D. A. Qin, C. C. Cheng, B. X. Chen, M. L. Hu, J. Molec. Struct., 1027 (2012) 104.
[3] X. Liu, Q. Gan, C. Feng, Inorg. Chim. Acta, 450 (2016) 299.
[4] N. Esfandiari, S. M. Ghoreishi, J. Supercritical Fluids, 84 (2013) 205.
[5] A. Yaraghi, O. M. Ozkendir, M. Mirzaei, Superlatt. Microstruct., 85 (2015) 784.
[6] M. Mirzaei, O. Gülseren, N. Hadipour, Comput. Theor. Chem. 1090 (2016) 67.
[7] W. Kan, X. Li, Eur. Polym. J., 49 (2013) 4167.
[8] M. O. Almeida, D. A. S. Barros, S. C. Araujo, S. H. D. M. Faria, V. G. Maltarollo, K. M. Honorio, Spectrochim. Acta Part A: Mol. Biomol. Spectros., 184 (2017) 169.
[9] A. Soltani, M. T. Baei, E. T. Lemeski, S. Kaveh, H. Balakheyli, J. Phys. Chem. Solids, 86 (2015) 57.
[10] K. Shayan, A. Nowroozi, Appl. Surf. Sci., 428 (2018) 500.
[11] C. Moisescu-Goia, M. Muresan-Pop, V. Simon, J. Molec. Struct., 1150 (2017) 37.
[12] A. Buczkowski, P. Urbaniak, H. Piekarski, B. Palecz, Spectrochi. Acta Part A: Molec. Biomolec. Spectros., 171 (2017) 401.
[13] M. A. Safwata, G. M. Solimana, D. Sayedc, M. A. Attia, Intern. J. Pharm., 513 (2016) 648.
[14] G. Chen, R. Gong, Saudi Pharma. J., 24 (2016) 250.
[15] H. H.-H. Lin, A. Y.-C. Lin, Water Res., 48 (2014) 559.
[16] A. Koltsakidou, M. Antonopoulou, E. Evgenidou, I. Konstantinou, A. E. Giannakas, M. Papadaki, D. Bikiaris, D. A. Lambropoulou, Sci. Total Environ., 578 (2017) 257.
[17] C. Gómez-Canela, G. Bolivar-Subirats, R. Tauler, S. Lacorte, J. Pharm. Biomed. Anal., 137 (2017) 33.
[18] H. Sh. Mohamed, A. R. A. Dahy, R.t M. Mahfouz, J. Pharm. Biomed. Anal., 145 (2017) 509.
[19] T. Kosjek, S. Perko, D. Zigon, E. Heath, J. Chromatogr. A, 1290 (2013) 62.
[20] W. Li, J. Tanumihardja, T. Masuyama, G. Korshin, J. Hazard. Mat., 282 (2015) 125.
[21] C. A. Lutterbeck, M. L. Wilde, E. Baginska, C. Leder, E. L. Machado, K. Kümmerer, Environ. Pollut., 208 (2016) 467.
[22] Y. Zhang, Y. Xiao, J. Zhang, V. W. C. Chang, T.-T. Lim, J. Environ. Chem. Eng., 5 (2017) 1133.
[23] H. K. Risinggard, S. Cooil, F. Mazzola, D. Hu, M. Kjærvik, E. R. Østlid, N. Patil, A. Preobrajenski, D. A. Evans, D. W. Breiby, T. T. Trinh, Justin W. Wells, Appl. Surf. Sci., 435 (2018) 1213.
[24] S. D. Bukkitgar, N. P. Shetti, Mat. Sci. Eng. C, 65 (2016) 262.
[25] S. Kurbanoglu, S. A. Ozkan, J. Pharm. Biomed. Anal., 147 (2018) 439.
[26] A. Shah, E. Nosheen, F. Zafar, S. N. uddin, D. D. Dionysiou, A. Badshah, Z.-ur-Rehman, G. S. Khan, J. Photochem. Photobiol. B: Biol., 117 (2012) 269.

Annals of the University of Craiova
The Chemistry Series
Volume XLV, No. 1 (2018) 18-29
homepage: chimie.ucv.ro/anale/

Investigating the manner in which a naphtoquinonic thiol coordinates to a metal center by using HOMO-LUMO methods

Research article

Liana Simona Sbîrnă[1], Sebastian Sbîrnă[2], Clementina Moldovan[3]*

[1] University of Craiova, Faculty of Sciences, Department of Chemistry, Calea București 107i, Craiova, Romania
[2] Alro S. A., Strada Pitești, 116, Slatina, Romania
[3] University of Petroșani, Faculty of Mining, Department of Management, Environmental Engineering and Geology, Strada Universității, 20, Petroșani, Romania
* E-mail: simona.sbirna@gmail.com

Received: 26.02.2018 / Accepted: 30.03.2018 / Published: 16.07.2018

Abstract
This work has as a main purpose establishing the actual coordination manner of a thiol from the 1,4-naphtoquinone series, namely 2-(1,3-diortotholilguanidin)-3-thio-1,4-naphtoquinone, denoted as DTGTNQ, to a Ni(II)/Co(II) metal center, by performing a quantum-mechanical study based on HOMO-LUMO methods. The experimental basis of this computational study is the UV-VIS spectral analysis (absorption maxima occurring in the electronic spectra of the free and coordinated ligand have been interpreted within the Extended Hückel Theory).

Keywords: naphtoquinonic thiols, bidentate ligands, square-plane complex compounds, HOMO-LUMO methods, HyperChem 8.0.10

1. INTRODUCTION

The complex compounds that this paper deals with are formed by a heterocyclic thiol of the 1,4-naphtoquinone series, with Ni(II) and Co(II).

Elemental analysis shows that these two complexes exhibit the general formula $[ML_2]$, where M denotes one of the previously mentioned transitional metal ions and L denotes the heterocyclic ligand. Both of them have been characterized by chemical analyses, UV, visible, IR, EPR and NMR spectral analyses, as well as by conductivity and magnetic susceptibility measurements. The complex compounds $[ML_2]$ are square-planar.

The point of this paper is to get information about the real coordination manner of 2-(1,3-diortotholilguanidin)-3-thio-1,4-naphtoquinone (denoted as DTGTNQ) to these two metal ions, by performing a comparative quantum-mechanical study of these absorption bands proper to the organic thiol and its two complexes – with Ni(II) and Co(II), based on HOMO-LUMO methods.

2. STRUCTURE MODELLING

The molecular geometry of the free organic ligand was optimized in the Molecular Mechanics approach (MM^+), the cartesian coordinates for all atoms being obtained by using HyperChem 8.0.10 (trial version) [5]. Figure 1 presents the structure of DTGTNQ obtained using this computational program.

The molecule contains six heteroatoms. There are three nitrogen atoms, but only one of them will prove itself to be important in our discussion, and that is the reason for which this particular one (directly linked to 1,4-naphtoquinone) will be simply denoted as N in the HOMO-LUMO expressions. There are also two oxygen atoms, which are not equivalent to one another, that will be named $O^{(1)}$ and $O^{(2)}$. The sulfur atom, being by itself, will be obviously called S.

The structure of the $[ML_2]$ complex compounds was also represented by using this program [5]. In order to give a clear information, the two identical ligands will be called *L* and *L′*. The following notations will be used: S_L, $S_{L'}$ - for the sulfur atoms in the first and in the second ligand; N_L, $N_{L'}$- for the nitrogen atoms directly linked to the heterocycles in the first and in the second ligand; $O_L^{(1)}$, $O_L^{(2)}$ - for the oxygen atoms in the first ligand and $O_{L'}^{(1)}$, $O_{L'}^{(2)}$ - for the oxygen atoms in the second one.

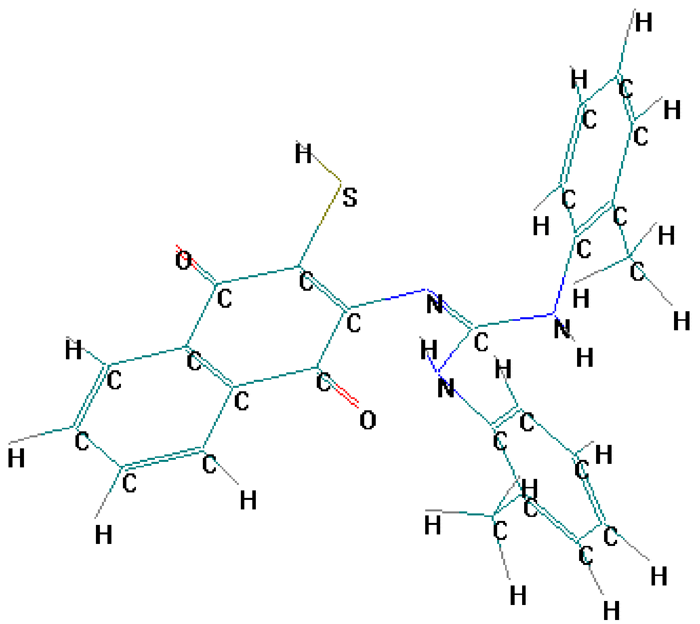

Figure 1. The structure of the free organic ligand DTGTNQ

3. HOMO-LUMO COMPUTATIONAL STUDY

In developing the HOMO-LUMO study, the depart point is to identify the "HOMO-LUMO" zone, *i.e.* the molecular orbitals (MO's) possibly involved in the coordination [1, 2]. This paper only presents the detailed study for the Ni(II) complex compound. For the other one (obtained by following the same HOMO-LUMO procedure), the final results are also reported.

Table 1 comparatively gives the energies and the occupation numbers for the most important MO's in the "HOMO-LUMO" zone for

the free ligand and the Ni(II) complex (the numbering is given by the ICONC program).

The cartesian coordinates for all the atoms were used into the ICONC program (an improved version of ICON [6, 7]).

The VSIP's and Slater exponents have been those recommended by ICONC library, apart from the VSIP's for the 4s, 4p and 3d levels for the metal ion, that would lead to the unacceptable conclusion that the σ coordinative bonding would have a "back-donation" character.

The EHT calculations were performed without iteration upon charge and configuration, the EHT practice showing that the results obtained in this way seem to be more reliable [6, 7].

Table 1. Energies and occupation numbers for the most important molecular orbitals of DTGTNQ and [Ni(DTGTNQ)$_2$]

DTGTNQ			[Ni(DTGTNQ)$_2$]		
Molecular orbital	ε (eV)	Occupation number	Molecular orbital	ε (eV)	Occupation number
ψ_{60}	-6.003				
ψ_{61}	-7.353		ψ_{121}	-5.994	0
ψ_{62}	-7.604	0	ψ_{122}	-6.002	
ψ_{68} (LUMO)	-10.477		ψ_{138}	-8.482	
ψ_{69} (HOMO)	-11.125		ψ_{143}	-11.249	
ψ_{70}	-11.250		ψ_{144}	-11.312	2
ψ_{71}	-11.584	2	ψ_{145}	-11.592	
ψ_{72}	-11.222		ψ_{146}	-11.655	
			ψ_{149}	-12.020	
			ψ_{150}	-12.218	

One must write down the expressions for the molecular wavefunctions that might be involved in the coordination – i.e. HOMO, LUMO and a few others, either occupied molecular orbitals having high energies or unoccupied molecular orbitals having low energies. These molecular wavefunctions have the following expressions for DTGTNQ, keeping the most important coefficients only (the p orbitals were simply denoted by x, y, z):

$\Psi_{60} \approx 0.2239\ p_x(O^{(1)}) + 0.17482\ p_y(O^{(1)}) + 0.2167\ p_x(O^{(2)}) + 0.1684\ p_y(O^{(2)})$

$\Psi_{61} \approx 0.1014\ p_x(S) + 0.1644\ p_x(N) + 0.1675\ p_y(N) - 0.2448\ p_z(N)$

$\Psi_{62} \approx 0.1004\ p_x(S) - 0.3145\ p_z(N)$

$\Psi_{68} \approx 0.3477\ p_x(S) + 0.2705\ p_y(S)$

$\Psi_{69} \approx 0.6062\ p_x(S) + 0.3812\ p_y(S) + 0.2371\ p_y(N)$

$\Psi_{70} \approx 0.2595\ p_x(O^{(1)}) - 0.3024\ p_y(O^{(1)}) - 0.2422\ p_z(O^{(1)}) - 0.2149\ p_x(O^{(2)}) + 0.3408\ p_y(O^{(2)}) + 0.2695\ p_z(O^{(2)})$

$\Psi_{71} \approx - 0.3611\ p_x(O^{(1)}) + 0.3925\ p_y(O^{(1)}) + 0.2585\ p_z(O^{(1)}) - 0.3572\ p_x(O^{(2)}) + 0.3692\ p_y(O^{(2)}) + 0.3415\ p_z(O^{(2)})$

$\Psi_{73} \approx 0.2353\ s(S) - 0.4181\ p_x(S) + 0.4611\ p_y(S) + 0.1334\ p_z(S)$

By following the same procedure, the expressions for the most important wavefunctions in the complex of DTGTNQ with Ni(II) were obtained (the p and d orbitals were simply denoted by x, y, z and z^2, x^2-y^2, xy, xz, yz respectively):

$\Psi_{121} \approx 0.1962\ p_x(O^{(1)}_{L'}) - 0.1923\ p_y(O^{(1)}_{L'}) + 0.2013\ p_x(O^{(2)}_{L'}) - 0.1774\ p_y(O^{(2)}_{L'})$

$\Psi_{122} \approx - 0.1912\ p_x(O^{(1)}_{L}) + 0.1865\ p_y(O^{(1)}_{L}) - 0.2017\ p_x(O^{(2)}_{L}) + 0.1763\ p_y(O^{(2)}_{L})$

$\Psi_{138} \approx 0.1434\ d_{xY}(Ni) + 0.2043\ d_{yz}(Ni)$

$\Psi_{143} \approx 0.1909\ p_x(O^{(1)}_{L}) + 0.2124\ p_z(O^{(1)}_{L}) - 0.2321\ p_x(O^{(2)}_{L}) - 0.1246\ p_y(O^{(2)}_{L}) - 0.3382\ p_z(O^{(2)}_{L}) - 0.1556\ p_x(O^{(1)}_{L'}) - 0.1950\ p_z(O^{(1)}_{L'}) + 0.2081\ p_x(O^{(2)}_{L'}) + 0.2961\ p_z(O^{(2)}_{L'})$

$\Psi_{144} \approx 0.1760\ p_x(O^{(1)}_{L}) + 0.2023\ p_z(O^{(1)}_{L}) + 0.2606\ p_x(O^{(2)}_{L}) - 0.1367\ p_y(O^{(2)}_{L}) - 0.2592\ p_z(O^{(2)}_{L}) + 0.1977\ p_x(O^{(1)}_{L'}) + 0.1005\ p_y(O^{(1)}_{L'}) + 0.2461\ p_z(O^{(1)}_{L'}) - 0.2574\ p_x(O^{(2)}_{L'}) - 0.1321\ p_y(O^{(2)}_{L'}) - 0.3109\ p_z(O^{(2)}_{L'})$

$\Psi_{145} \approx -0.3053\ p_x(O_L^{(1)}) - 0.2586\ p_y(O_L^{(1)}) - 0.3793\ p_z(O_L^{(1)}) - 0.1778\ p_x(O_L^{(2)}) - 0.2832\ p_z(O_L^{(2)}) + 0.2474\ p_x(O_{L'}^{(1)}) + 0.1979\ p_y(O_{L'}^{(1)}) + 0.3415\ p_z(O_{L'}^{(1)}) + 0.1488\ p_x(O_{L'}^{(2)}) + 0.2572\ p_z(O_{L'}^{(2)})$

$\Psi_{146} \approx -0.2718\ p_x(O_L^{(1)}) - 0.1949\ p_y(O_L^{(1)}) - 0.2985\ p_z(O_L^{(1)}) - 0.1915\ p_x(O_L^{(2)}) + 0.1264\ p_y(O_L^{(2)}) - 0.2445\ p_z(O_L^{(2)}) - 0.3041\ p_x(O_{L'}^{(1)}) - 0.2005\ p_y(O_{L'}^{(1)}) - 0.3732\ p_z(O_{L'}^{(1)}) - 0.2043\ p_x(O_{L'}^{(2)}) - 0.1376\ p_y(O_{L'}^{(2)}) - 0.3160\ p_z(O_{L'}^{(2)})$

$\Psi_{149} \approx -0.1900\ p_z(S_L) + 0.1991\ p_x(S_{L'}) - 0.1631\ p_y(S_{L'})$

$\Psi_{150} \approx -0.1337\ p_y(S_L) + 0.1472\ p_z(S_L) + 0.1517\ p_z(S_{L'})$

4. ASSIGNMENTS OF THE ELECTRONIC TRANSITIONS

All the expressions previously presented constitute the theoretical basis for performing the most probable assignments for the absorption maxima occurring in the UV-VIS spectra of DTGTNQ and [Ni(DTGTNQ)$_2$].

In assigning these transitions, HOMO-LUMO methods have been applied. Beside the energetic criteria, the "zonal criteria" was taken into account.

According to this criteria [3, 4], it is very less probable for a transition to occur between two molecular orbitals practically localized on heteroatoms situated in two completely different areas of the quantum system. At contrary, it is correct to presume that is possible for a maximum to be attributed to a transition involving lone pairs of the same heteroatom, even though this particular one might not exhibit a great compatibility with the experiment [3, 4].

The most probable assignments for the transitions corresponding to the free and coordinated ligand are summarized in tables 2 - 4.

The first absorption maximum in order of increasing energy (at 700 nm) in the electronic spectrum of DTGTNQ is assigned to a transition between Ψ_{73} and Ψ_{68} (LUMO), *i.e.* two molecular orbitals of the sulfur atom. The second and third ones (at 367 and 324 nm) are

attributed to transitions between molecular orbitals for which the sulfur and nitrogen atoms play the most important role, specifically from Ψ_{69} (HOMO) to Ψ_{62} and Ψ_{61} respectively. The last two maxima (at 243 and 221 nm) are attributed to a couple of transitions from Ψ_{70} and Ψ_{71} to Ψ_{74}, all three of them being molecular orbitals actually localized on the two oxygen atoms from the carbonyl groups of 1,4-naphtoquinone.

Table 2. The assignments for the electronic absorption bands of the free ligand, DTGTNQ

Electronic transition ($\Psi \rightarrow \Psi^*$)	E^{Ψ} (eV)	E^{Ψ^*} (eV)	Δ_E (eV)	λ (nm)	λ_{exp} (nm)
$\Psi_{73}(S) \rightarrow \Psi_{68}(S)^{LUMO}$	-12.222	-10.477	1.745	710	700
$\Psi_{69}(S,N)^{HOMO} \rightarrow \Psi_{62}(S,N)$	-11.125	-7.604	3.521	352	367
$\Psi_{69}(S,N)^{HOMO} \rightarrow \Psi_{61}(S,N)$	-11.125	-7.353	3.772	329	324
$\Psi_{70}(O^{(1)},O^{(2)}) \rightarrow \Psi_{60}(O^{(1)},O^{(2)})$	-11.250	-6.003	5.247	236	243
$\Psi_{71}(O^{(1)},O^{(2)}) \rightarrow \Psi_{60}(O^{(1)},O^{(2)})$	-11.584	-6.003	5.581	222	221

Table 3. The assignments for the electronic absorption bands of the complex compound $[Ni(DTGTNQ)_2]$

Electronic transition ($\Psi \rightarrow \Psi^*$)	E^{Ψ} (eV)	E^{Ψ^*} (eV)	Δ_E (eV)	λ (nm)	λ_{exp} (nm)
$\Psi_{149}(S_L,S_{L^1}) \rightarrow \Psi_{138}(Ni)$	-12.020	-8.482	3.538	350	352
$\Psi_{150}(S_L,S_{L^1}) \rightarrow \Psi_{138}(Ni)$	-12.218	-8.482	3.736	332	330
$\Psi_{143}(O_L^{(1)},O_L^{(2)},O_{L^1}^{(1)},O_{L^1}^{(2)}) \rightarrow \Psi_{122}(O_L^{(1)},O_L^{(2)})$	-11.249	-6.002	5.247	236	242
$\Psi_{144}(O_L^{(1)},O_L^{(2)},O_{L^1}^{(1)},O_{L^1}^{(2)}) \rightarrow \Psi_{122}(O_L^{(1)},O_L^{(2)})$	-11.312	-6.002	5.310	233	242
$\Psi_{143}(O_L^{(1)},O_L^{(2)},O_{L^1}^{(1)},O_{L^1}^{(2)}) \rightarrow \Psi_{121}(O_{L^1}^{(1)},O_{L^1}^{(2)})$	-11.249	-5.994	5.255	236	242

$\Psi_{144}(O^{(1)}_{L},O^{(2)}_{L},O^{(1)}_{L^1},O^{(2)}_{L^1}) \rightarrow \Psi_{121}(O^{(1)}_{L^1},O^{(2)}_{L^1})$	-11.312	-5.994	5.318	233	242
$\Psi_{145}(O^{(1)}_{L},O^{(2)}_{L},O^{(1)}_{L^1},O^{(2)}_{L^1}) \rightarrow \Psi_{122}(O^{(1)}_{L},O^{(2)}_{L})$	-11.592	-6.002	5.590	222	221
$\Psi_{146}(O^{(1)}_{L},O^{(2)}_{L},O^{(1)}_{L^1},O^{(2)}_{L^1}) \rightarrow \Psi_{122}(O^{(1)}_{L},O^{(2)}_{L})$	-11.655	-6.002	5.653	219	221
$\Psi_{145}(O^{(1)}_{L},O^{(2)}_{L},O^{(1)}_{L^1},O^{(2)}_{L^1}) \rightarrow \Psi_{121}(O^{(1)}_{L^1},O^{(2)}_{L^1})$	-11.592	-5.994	5.598	221	221
$\Psi_{146}(O^{(1)}_{L},O^{(2)}_{L},O^{(1)}_{L^1},O^{(2)}_{L^1}) \rightarrow \Psi_{121}(O^{(1)}_{L^1},O^{(2)}_{L^1})$	-11.655	-5.994	5.661	219	221

Table 4. The assignments for the electronic absorption bands of the complex compound [Co(DTGTNQ)$_2$]

Electronic transition ($\Psi \rightarrow \Psi^*$)	E^{Ψ} (eV)	E^{Ψ^*} (eV)	Δ_E (eV)	λ (nm)	λ_{exp} (nm)
$\Psi_{149}(S_L,S_{L^1}) \rightarrow \Psi_{137}(Co)$	-12.050	-8.632	3.418	363	370
$\Psi_{151}(S_L,S_{L^1}) \rightarrow \Psi_{137}(Co)$	-12.257	-8.632	3.625	342	340
$\Psi_{143}(O^{(1)}_{L},O^{(2)}_{L},O^{(1)}_{L^1},O^{(2)}_{L^1}) \rightarrow \Psi_{122}(O^{(1)}_{L},O^{(2)}_{L})$	-11.262	-6.003	5.259	235	242
$\Psi_{144}(O^{(1)}_{L},O^{(2)}_{L},O^{(1)}_{L^1},O^{(2)}_{L^1}) \rightarrow \Psi_{122}(O^{(1)}_{L},O^{(2)}_{L})$	-11.313	-6.003	5.310	233	242
$\Psi_{143}(O^{(1)}_{L},O^{(2)}_{L},O^{(1)}_{L^1},O^{(2)}_{L^1}) \rightarrow \Psi_{121}(O^{(1)}_{L^1},O^{(2)}_{L^1})$	-11.262	-5.993	5.269	235	242
$\Psi_{144}(O^{(1)}_{L},O^{(2)}_{L},O^{(1)}_{L^1},O^{(2)}_{L^1}) \rightarrow \Psi_{121}(O^{(1)}_{L^1},O^{(2)}_{L^1})$	-11.313	-5.993	5.320	233	242

$\Psi_{145}(O_L^{(1)}, O_L^{(2)}, O_{L^1}^{(1)}, O_{L^1}^{(2)}) \rightarrow \Psi_{122}(O_L^{(1)}, O_L^{(2)})$	-11.599	-6.003	5.596	222	221
$\Psi_{146}(O_L^{(1)}, O_L^{(2)}, O_{L^1}^{(1)}, O_{L^1}^{(2)}) \rightarrow \Psi_{122}(O_L^{(1)}, O_L^{(2)})$	-11.662	-6.003	5.659	219	221
$\Psi_{145}(O_L^{(1)}, O_L^{(2)}, O_{L^1}^{(1)}, O_{L^1}^{(2)}) \rightarrow \Psi_{121}(O_{L^1}^{(1)}, O_{L^1}^{(2)})$	-11.599	-5.993	5.606	221	221
$\Psi_{146}(O_L^{(1)}, O_L^{(2)}, O_{L^1}^{(1)}, O_{L^1}^{(2)}) \rightarrow \Psi_{121}(O_{L^1}^{(1)}, O_{L^1}^{(2)})$	-11.662	-5.993	5.669	219	221

As far as the electronic spectrum of the Ni(II) complex is concerned, one may see that the first and the second absorption maxima in order of increasing energy (at 352 and 330 nm) are assigned to the transitions from the molecular orbitals Ψ_{149} and Ψ_{150} (on the sulfur atoms) to the molecular orbital Ψ_{138} (on the transitional metal ion), that is to say that they are due to charge-transfer bands ($L \rightarrow M$).

The next two maxima are both attributed to transitions between molecular orbitals for which the oxygen atoms play the most important role. Explicitly, the maximum at 242 nm is assigned to a quartet of transition from the occupied molecular orbitals Ψ_{143} and Ψ_{144} to the unoccupied molecular orbitals Ψ_{121} and Ψ_{122}, whereas the maximum at 221 nm is assigned to a quartet of transition from the occupied molecular orbitals Ψ_{144} and Ψ_{145} to the same couple of occupied molecular orbitals, namely Ψ_{121} and Ψ_{122}.

On this basis, we are now able to provide the real coordination manner of the investigated ligand to Ni(II) and Co(II).

The fact that the first, the second and the third maxima in the electronic absorption spectrum free organic thiol are not found again in the one of the complex compound with Ni(II) shows that the sulfur atom of each thiol is involved in the coordination and suggests that the nitrogen atom also participates to the chemical bond.

The participation of the sulfur atoms S_L, $S_{L'}$ to the coordination process is also sustained by the interpretation of the first and the second maxima in the UV-VIS spectrum of the complex as being due to a

charge-transfer process L → M involving as occupied molecular orbitals two orbitals for which the sulfur atoms from both identical ligands play a main part.

The fact that the four oxygen atoms have obviously nothing to do with the coordination process also leads to the idea that the nitrogen atoms N_L, $N_{L'}$ are involved in the coordination.

This can easily be seen by comparing the last two absorption maxima in the complex with the similar ones in the free ligand.

Not only the values of wavelengths are quite the same, but also the interpretation is quite identical. There are exclusively molecular orbitals in which atomic orbitals from $O_L^{(1)}$, $O_L^{(2)}$, $O_{L'}^{(1)}$, $O_{L'}^{(2)}$ play the main part involved in these transitions.

Moreover, there is an obvious link between the molecular orbitals involved in the transitions from the spectrum recorded for DTGTNQ and the molecular orbitals involved in the transitions from the spectrum recorded for [Ni(DTGTNQ)$_2$].

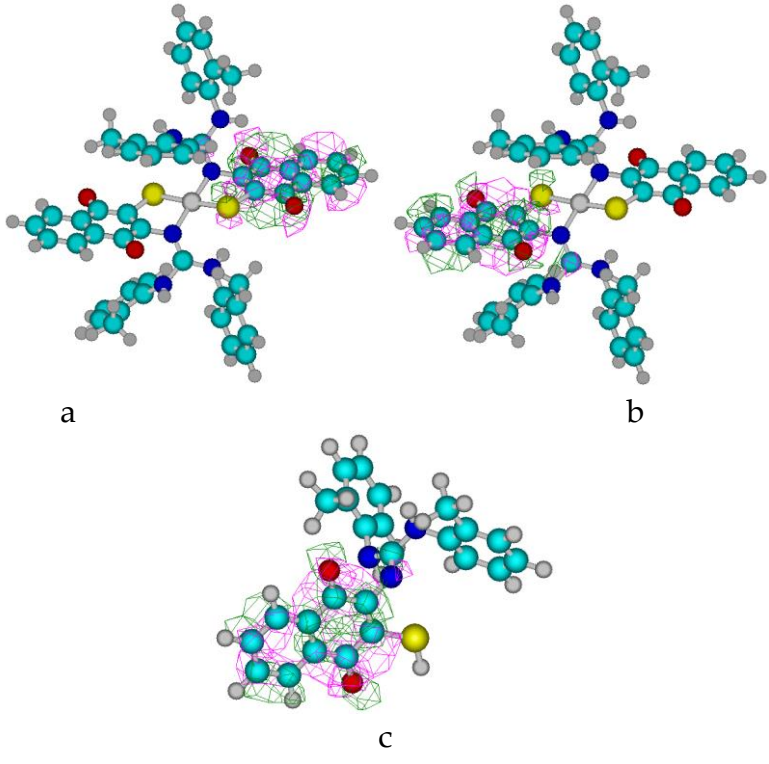

Figure 2. The molecular orbitals Ψ_{121} (a) and Ψ_{122} (b) of [Ni(DTGTNQ)$_2$] compared to the corresponding molecular orbital, Ψ_{60}, of DTGTNQ (c)

It can be point out that the orbitals Ψ_{121} and Ψ_{122} of the complex (whose energies are -5.994 eV and -6.002 eV respectively) are in fact exactly the two Ψ_{60} molecular orbitals of the two identical free ligands (the energy is -6.003 eV), as it might be seen from figures 2a-c [5]. Explicitly, figures 2a and 2b present the couple of molecular orbitals Ψ_{121} and Ψ_{122} in complex, whereas figure 2c shows the former Ψ_{60} molecular orbital in the thiol that can be found again, twice of course, in the complex compound.

In the same way, there can be seen an obvious correspondence between (Ψ_{143}, Ψ_{144}) and the former Ψ_{70} and also between (Ψ_{145}, Ψ_{146}) and the former Ψ_{71}.

An absolutely similar discussion leads to the results for the complex compound formed by DTGTNQ with Co(II).

5. CONCLUSIONS

The absorption maxima occurring in the electronic spectra of the free heterocyclic ligand DTGTNQ and the [M(DTGTNQ)$_2$] complexes, where M = Ni(II) and Co(II), have been compared and interpreted by using HYPERCHEM 8.0.10 (trial version) and ICON-EDit/BICON-CEDiT programs.

Extended Hückel Theory (EHT) calculations have been made and, finally, HOMO-LUMO methods have been applied, as it was mentioned above.

The HOMO-LUMO methods lead to the clear conclusion that the sulfur atom plays a key role in the coordination process, whereas the oxygen atom plays no part in it.

Consequently, the coordination is realized by means of nitrogen and sulfur, so that DTGTNQ is proved to act as a bidentate (N, S) ligand that combines with Ni(II) and Co(II) in a 2:1 ratio.

The paper proves that the electronic transitions in the spectrum of DTGTNQ (occurring, of course, between molecular orbitals belonging to the HOMO-LUMO zone) are due to charge transfer involving electron lone pairs of sulfur and nitrogen.

References

[1] A. Ramazani, M. Sheikhi, Y. Hanifehpour et al., *J. Struct. Chem.* 59 **(2018)** 529. https://doi.org/10.1134/S0022476618030058.

[2] R. Ghiasi, *Struct. Chem*. 25 **(2014)** 829. https://doi.org/10.1007/s11224-013-0345-7.

[3] V. M. Arsovski, B. Đ. Božić, J. M. Mirković et al., *J. Mol. Model.* 20 **(2014)** 2384. https://doi.org/10.1007/s00894-014-2384-4.

[4] K. Biernacki, A. L. Magalhães, C. Freire et al., *Struct. Chem*. 22 **(2011)** 697. https://doi.org/10.1007/s11224-011-9748-5.

[5] http://www.hyper.com/

[6] http://home.iitk.ac.in/

[7] https://calzaferri.dcb.unibe.ch/program/iconedit.html

Annals of the University of Craiova
The Chemistry Series
Volume XLV, No. 1 (2018) 30-38
homepage: chimie.ucv.ro/anale/

A three-component reaction in a heterogeneous medium to obtain aromatic aldehydes

Research article

George Brătulescu[1], Cecil Sorin Mirea[2], Simona Daniela Neamțu[2], Lucrețiu Radu[2], Carmen Valeria Albu[2], Cristina Georgeanu[2]*

[1] University of Craiova, Faculty of Sciences, Department of Chemistry, Calea București 107i, Craiova, Romania
[2] University of Medicine and Pharmacie, Petru Rares Street no 2, Craiova, Romania
*E-mail: gbratulescu@gmail.com

Received: 16.03.2018 / Accepted: 24.04.2018 / Published: 16.07.2018

Abstract
A mild method for obtaining aromatic aldehydes in a heterogeneous medium is depicted. The starting substances were halogenated compounds. The oxidation reaction was carried out with dimethyl sulfoxide (DMSO) in the presence of solid potassium bicarbonate as the inorganic base and in the absence of any added solvent. The chemical process is a soft alternative to the preparation of aromatic aldehydes. The structure of aromatic aldehydes was confirmed by measurements of physical constants and organic structural analysis.

Keywords: heterogeneous medium, aromatic aldehydes, organic halides; oxidation, DMSO

1. INTRODUCTION

Aromatic aldehydes play an important role in organic chemistry for development of synthetic compounds and theoretical studies as well. Aromatic aldehydes carrying supplementary substituents are versatile reagents in medicinal chemistry and organic synthesis [1-3]. Quantities of many aromatic aldehydes such as vanillin, veratraldehyde, are found in essential oils, causing specific smells [4].

The formylation of aromatic hydrocarbons with Lewis acids is not a method of preparing aromatic aldehydes since formyl halides could not be prepared. Preparation of aromatic aldehydes by Casiraghi [5] and Duff [6] methods involves hydroxymethyl- or halomethyl-substituted aromatic compounds which are oxidized to aromatic aldehydes.

A useful method for introducing the formyl group into an aromatic ring employs the Gattermann-Koch reaction between CO, HCl and ArH catalyzed by a Friedel-Crafts catalyst (eg, $AlCl_3$) or involves the formylation system HCN or $Zn(CN)_2$ [7].

An industrial proceeding to get aromatic aldehydes make use of 1,3,5-triazine and a strong Bronsted acid such as HCl/Et_2O or $AlCl_3$ as the formylating system [8,9].

The *o*-hydroxy aromatic aldehydes were obtained using the Reimer-Tiemann reaction which involves $CHCl_3$/KOH as formylation reactants of the aromatic ring of phenols and naphthols [10].

The Vilsmeier-Haack reaction allows obtaining of the aromatic aldehydes from *N*,*N*-dimethylformamide (DMF), phosphorus oxychloride ($POCl_3$) and an electron-rich aromatic hydrocarbon. The electrophilic reactant is a substituted chloroiminium cation, also named the Vilsmeier reagent, that results from the reaction between DMF and $POCl_3$ [11]. This method is currently used on industrial scale.

Rieche formylation is a reaction discovered in 1960. An electron rich aromatic compound reacts with dichloromethyl methyl ether in presence of titanium tetrachloride as catalyst in acidic pH [12, 13].

Kornblum oxidation allows the synthesis of aldehydes starting from a primary halide and dimethyl sulfoxide (DMSO). The classical method takes place in a homogeneous medium, the organic solution.

Tertiary amine or pyridine are often used as organic base catalysts for scavenging HX (Scheme 1) [14].

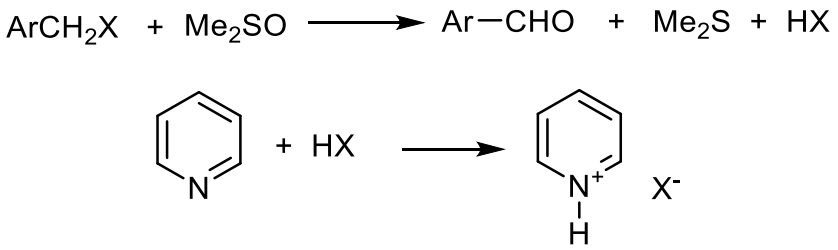

Scheme 1. Kornblum oxidation in classical approach

A significant drawback of the conventional Kornblum oxidation is the long reaction time to obtain a convenient yield [14]. However, some benefits were obtained using electromagnetic microwaves as the source of activation for this reaction [15].

2. MATERIALS AND METHODS

2.1. Materials

The organic primary halides, DMSO and potassium bicarbonate are commercially substances.

The IR/FT spectra were recorded using an Alpha Bruker Optics spectrometer.

The UV-VIS spectra were recorded in MeOH as a solvent using a Varian Cary spectrometer.

An Abbe refractometer was used for determination of the refractive index.

The boiling points were measured by distillation.

The melting points were measured with the help of a Gallenkamp digital melting point apparatus.

The electron impact mass spectrum of 4-(*N,N*-dimethylamino) benzaldehyde was obtained with a Nermarg R10-10 spectrometer.

2.2. Methods

Experimental protocol

As a standard example, the method of obtaining benzaldehyde: A stove-dried, 50 mL one-necked, round-bottomed flask equipped with an egg-shaped magnetic stirring bar and a reflux condenser was charged with DMSO (12 mmol), potassium bicarbonate (25 mmol) and benzyl bromide (9 mmol) added drop-wise. The mixture was placed into a water bath on a magnetic stirrer hot plate and stirred at room temperature for 8 hours. The resulting mixture was poured into ice-water (75 mL) and extracted with 2x20 mL of ether. The joined ethereal extracts were dried over anhydrous sodium sulfate and the resulting mixture was filtered. Concentration of the filtrate gives the benzaldehyde. yield 50%. (b.p.= 178-179 °C, refractive index 1.545, density 1.04 g/mL). The pure product exhibits the same properties as the commercial product of Sigma-Aldrich. Synthesis of other compounds was achieved by the same protocol (Table 1).

3. RESULTS AND DISCUSSION

We synthesized aromatic aldehydes with the help of the Kornblum oxidation. The amine base catalyst used in the conventional Kornblum reaction was replaced with a mineral solid base, potassium bicarbonate. As a result of this change, the reaction takes place via a one-pot three-component reaction in a heterogeneous medium without solvent. Aromatic aldehyde is produced by a reaction taking place on the surface of the solid potassium bicarbonate granule by a lower energy transition state. One way to increase the nucleofugacity of halides is to use bicarbonate anion. The first step is a S_N2 displacement of the halide anion. This oxidation mechanism has been previously discussed and is shown below in Scheme 2 [15].

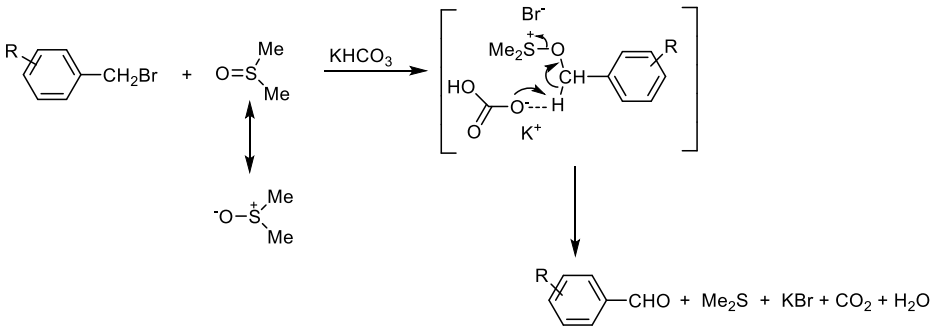

Scheme 2. Mechanism of reaction of aryl aldehydes synthesis

Due to the heterogeneous medium and the sequential way of combining the reagents, the yield and selectivity are improved. The Kornblum oxidation occurs in a glass reaction vessel provided with a reflux cooler and a stirrer.

The structure of the aromatic aldehyde was confirmed by measuring the boiling temperature or melting temperature, the IR spectrum, the UV spectrum and the refractive index. The compounds obtained using this protocol are outlined in Table 1.

The vibrational spectra (IR) of the aromatic aldehydes were recorded in the 4000-500 cm^{-1} reciprocal centimeters range ($\tilde{\nu}$) (Figure 1) [16]. The characteristic stretching (valence) vibration of the formyl group (CHO) is found in the 1683-1700 cm^{-1} wavelength range. The the specific infrared absorption band of the formyl group is very intense and demonstrates the aromatic aldehyde formation at the end of the chemical reaction. Low intensity absorption bands in the 2898-2990 cm^{-1} region of the IR spectrum (compound 3 and 4, Table 1) are assigned to the asymmetric stretching vibration of methylenic group, ν^{asym}_{CH2}. The medium intensity absorption bands which occur at 2790-2810 cm^{-1} belong to symmetric valency vibration of methylenic group, ν^{sym}_{CH2}. The very weak bands at 3010-3070 cm^{-1} are due to the stretching of the C-H covalent bonds in the aromatic rings. The covalent C-H bond in the formyl group (-CHO) has its stretching vibration in the reciprocal centimeters range of 2690-2700 cm^{-1}.

The ultraviolet-visible absorption spectra of aromatic aldehydes (Figure 2) are interesting because they provide the presence of the formyl group in the substance [16]. All products absorb UV waves thanks to the transition of electrons between the highest occupied

molecular orbital (HOMO) and the highest unoccupied molecular orbital (LUMO). Electronic transitions $\pi \rightarrow \pi^*$ have the maximum absorption λ_{max} in the ultraviolet range 206-250 nm. Electronic transitions $n \rightarrow \pi^*$ exhibit the highest absorption bands λ_{max} in the wavelength range of 254-350 nm.

Table 1. Aromatic aldehydes synthesized by Kornblum's oxidation

$Ar\text{-}CH_2X + Me_2SO + KHCO_3 \rightarrow Ar\text{-}CHO + Me_2S + KX + H_2O + CO_2$

N°	Compounds/Formula	B.p./M.p [°C]	Yield [%]	IR $\tilde{\nu}$ [cm^{-1}] CH=O	UV λ_{max}[nm] Ar-CH=O
1	Benzaldehyde C_6H_5CHO	B.p.178-179	50	1700 vs	244($\pi \rightarrow \pi^*$) 280($n \rightarrow \pi^*$)
2	4-Chlorobenzaldehyde *p*-ClC_6H_4CHO	M.p.49-50	44	1694 vs	206($\pi \rightarrow \pi^*$) 254($n \rightarrow \pi^*$)
3	2-Methylbenzaldehyde *o*-$CH_3C_6H_4CHO$	B.p.201-202	48	1698 vs	250($\pi \rightarrow \pi^*$) 294($n \rightarrow \pi^*$)
4	4-(Dimethylamino) benzaldehyde *p*-$(CH_3)_2NC_6H_4CHO$	M.p.73-74	53	1683 s	242($\pi \rightarrow \pi^*$) 340($n \rightarrow \pi^*$)
5	2-Chlorobenzaldehyde *o*-ClC_6H_4CHO	B.p.209-210	46	1699 vs	246($\pi \rightarrow \pi^*$) 292($n \rightarrow \pi^*$)

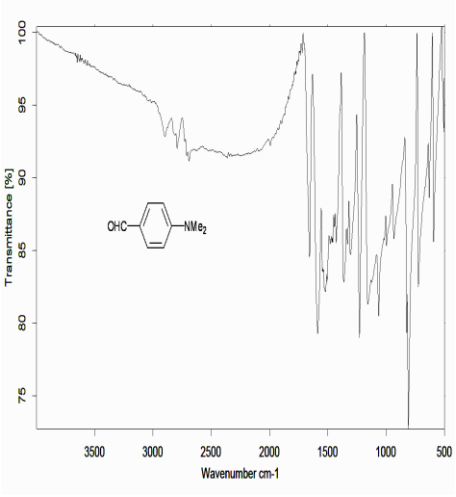

Figure 1. The infrared spectrum of 4-(*N,N*-dimethylamino) benzaldehyde.

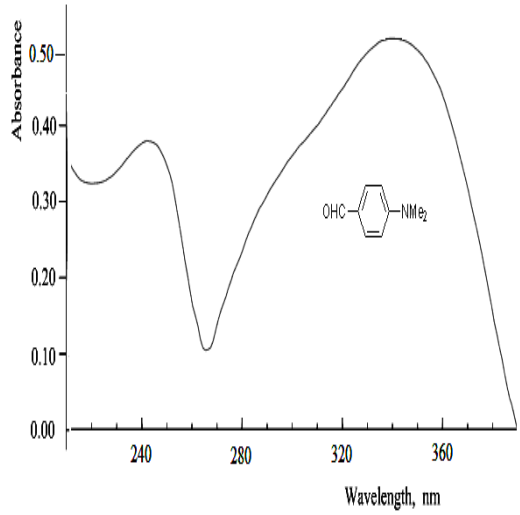

Figure 2. The electronic spectrum of 4-(*N,N*-dimethylamino) benzaldehyde in MeOH.

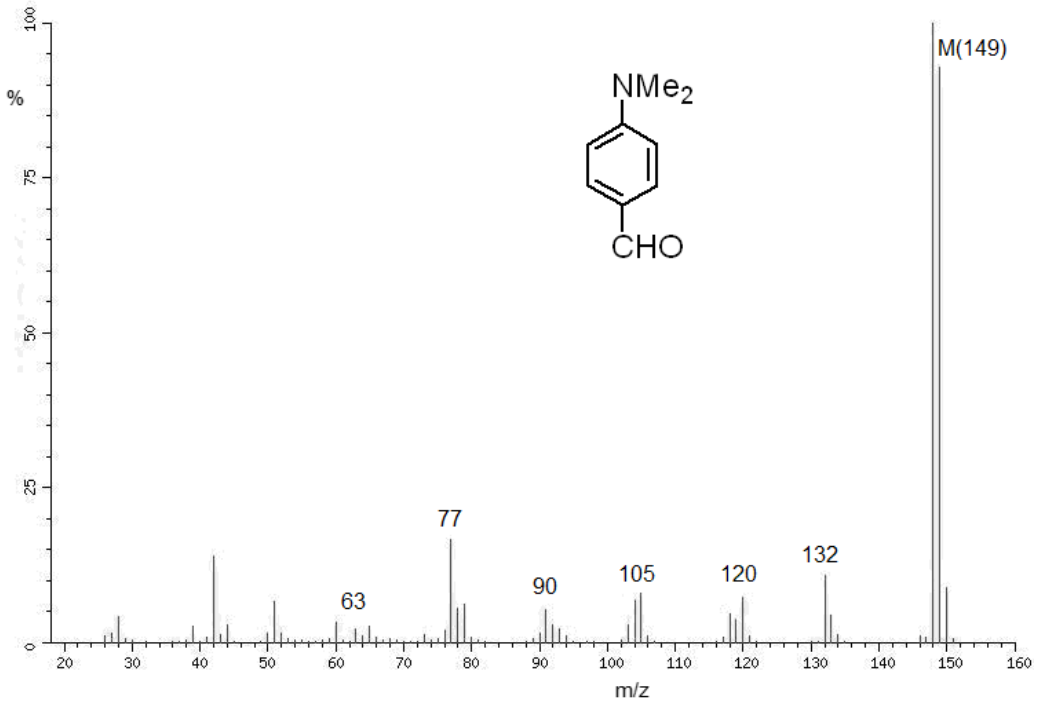

Figure 3. Electron impact mass spectrum of 4-(*N*,*N*-dimethylamino) benzaldehyde.

In the electron impact mass spectrum of 4-(*N*,*N*-dimethylamino) benzaldehyde (Figure 3), the presence of the molecular ion peak is observed at m/z=149. This peak is assigned to the unfragmented radical cation $M^{+\cdot}$ and it's the parent's peak or the molecular ion [16]. Very weak peak (m/z=150) near the parent ion peak is a satellite peak (M+1) that is due to the isotopic distribution of the elements in 4-(*N*,*N*-dimethylamino) benzaldehyde. We notice the peak of molecular ion and the base peak (I%=100) is not the same. The base peak corresponds to m/z=148. We have found three ways of fragmentation of molecular ion of the compound (A, B, C, Scheme 3).

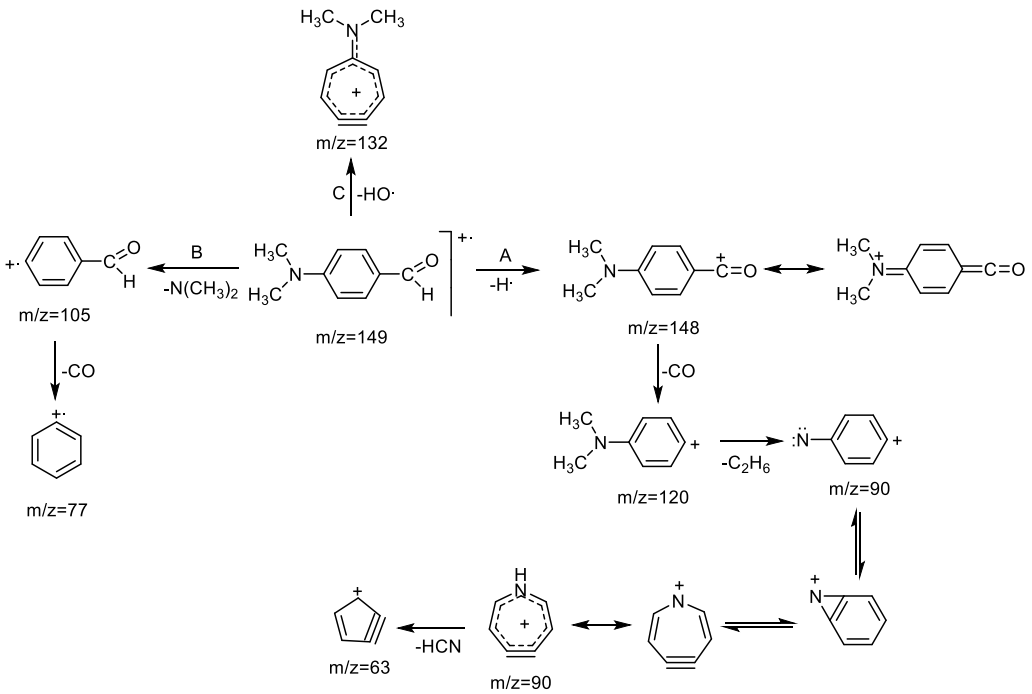

Scheme 3. Mechanism of fragmentation of molecular ion of 4-(*N*,*N*-dimethylamino) benzaldehyde.

In the first fragmentation pathway (A), the molecular radical cation $M^{+\cdot}$of *p*-(*N*,*N*-dimethylamino) benzaldehyde loses a hydrogen atom of the formyl group and forms a very stable radical cation of (4-(dimethylamino)phenyl)(oxo)methylium (m/z=148). Then, the leakage of a carbon monoxide molecule produces the (dimethylamino) phenyl radical cation (m/z=120). An ethane elimination generates the radical cation of the nitrene (m/z=90), which isomerizes to 7-aza-cyclohepta-2,6-dien-4-yn-1-ylium cation, and then, by a loss of hydrogen cyanide, gives cyclopent-2-en-4-yn-1-ylium cation (m/z=63).

In the second fragmentation pathway (B), the molecular ion $M^{+\cdot}$of *p*- (*N*,*N*-dimethylamino) benzaldehyde releases a molecule of dimethylamine to form the benzaldehyde radical cation (m/z=105). Furthermore, the latter losses a molecule of carbon monoxide and forms the phenyl radical cation (m/z=77).

The third fragmentation pathway (C) leads to the charge-delocalized cation *N*-(cyclohepta-2,6-dien-4-yn-1-ylidene)-*N*-methylmethanaminium (or (*N*,*N*-dimethylamino)cyclohepta-2,6-dien-4-

yn-1-yl carbocation) with m/z=132 by loss of a hydroxyl radical in the molecular ion. Having an electronic structure in which the positive charge is delocalized to eight atoms, this cation has an important relative abundance in the mass spectrum of the compound. In any case, this cation m/z=132 (pathway C) is more stable than the cation m/z=90 (pathway A) as it results from the height of their peaks.

4. CONCLUSIONS

Aromatic aldehydes can be synthesized by Kornblum oxidation in a one-pot reaction involving an aromatic halocarbon, DMSO and potassium bicarbonate as proton acceptor. The reaction takes place in a heterogeneous environment at room temperature and without solvent. The chemical structure of the aromatic aldehydes are confirmed by structural analysis.

References

[1] A. R. Katritzky, H. Y. He, Q. Long, X. Cui, J. Level, A. L. Wilcox, *ARKIVOC*, III (**2000**) 240.
[2] W. Kantlehner, *Eur. J. Org. Chem*., 14 (**2003**) 2530.
[3] C. Stephane, W.D. Robert, G.R. Sally, A.R. John, H.B.R. David, *Chem. Rev*. 106 (**2006**) 2943.
[4] M. Brenes, A. García, P. García; J. J. Rios; A. Garrido, *J. Agric. Food. Chem*., 47 (**1999**) 3535.
[5] N. U. Hofslokken, L. Skatebol, *Acta Chem. Scand*., 53 (**1999**) 258.
[6] G. J. Hollingworth, "Comprehensive Organic Functional Group Transformations" (Ed.: G. Pattenden), Pergamon, Oxford, New York, Tokyo, **1995**, vol. 3, p. 91.
[7] L. Gattermann, J. A. Koch, *Ber*., 30 (**1897**) 1622
[8] A. Kreutzberger, *Angew. Chem., Int. Ed*., 6 (**1967**) 940.
[9] A. V. Aksenov1, I. V. Aksenova, *Chem. Heterocycl. Compd*., 45 (**2009**) 130.
[10] H. Wynberg, *Chem.Rev*., 60 (**1960**) 169.
[11] A. Vilsmeier, A. Haack, *Chem. Ber*., 60 (**1927**) 119.
[12] A. Rieche, H. Gross, E. Höft, *Chem. Ber*., 93 (**1960**) 88.
[13] H. Gross, I. Farkas, R. Bognar, *Z. Chem*., 18 (**1978**) 18, 201.
[14] N. Kornblum, W. J. Jones, G. J. Anderson, *J. Am. Chem. Soc*., **81** (**1959**) 4113.
[15] G. Brătulescu, *Synth. Commun*., **38** (**2008**) 2748.
[16] G. Brătulescu, "Introducere în spectroscopia compuşilor organici", Ed. Sitech, Craiova, **2008**.

Annals of the University of Craiova
The Chemistry Series
Volume XLV, No. 1 (2018) 39-45
homepage: chimie.ucv.ro/anale/

Contribution to Co(III) nitrocomplexes chemistry. New analogues of $NH_4[Co(NO_2)_4(NH_3)_2]$ complex with hexamethylenetetramine

Research article

Anca Gănescu[1], Florina Ciolan[1], Elena Ionescu[2], Adina Dorina Glodeanu[2], Simona Daniela Neamțu[2], Cecil Sorin Mirea[2], Lucrețiu Radu[2], Carmen Valeria Albu[2], Cristina Georgmăneanu[2]*

[1] University of Craiova, Faculty of Sciences, Department of Chemistry, Calea București 107i, Craiova, Romania
[2] University of Medicine and Pharmacie, Petru Rares Street no 2, Craiova, Romania
* E-mail: anca_ganescu@yahoo.com

Received: 05.04.2018 / Accepted: 07.05.2018/ Published: 16.07.2018

Abstract
The work presents experimental data about new analogues of ammonium tetranitro-diamineCo(III) complex (Erdmann complex) with hexamethylenetetramine (hta).The base complex obtained $NH_4[Co(NO_2)(hta)_2]$, as well as the Erdmann complex present practical importance for agriculture. They contain nitrogen under cationic, anionic and molecular form and Co(III) as micronutrient and can serve as source of other micronutrients through replacement of NH_4 with other complexes cations. Some of these complexes are soluble in water, others are hardly soluble and nonhygroscopic. Their efficiency in fertilizing was demonstrated by us experimentally.

Keywords: Co (III), nitrocomplexes, hexamethylenetetramine, micronutrients

1. INTRODUCTION

There exists a wide range of complexes of nitroamine [1,2,3] as tetranitro-diamine ammonium Co(III) complex, a compound which was obtained for the first time by Erdmann [2]. This complex can serve as a fertilizer because it contains nitrogen and an element that can be a micronutrient. It has, however some disadvantages, we have extended the Co(III) nitrocomplexes series with fertilizing action to new nitrocomplexes with the general formula $(NH_4)_{n-3}[Co(NO)_{6-n}(N_4C_6H_{12})_n]$, where $N_4C_6H_{12}$ in hexamethylenetetramine noted hta [2,3] and n las the values of 2 or 3. These complexes are microcrystalline substances, partially in water, with red or yellow-orange colour. They decompose only at temperature between 138-175 °C staring from the base complex with two molecules of hta we have obtained a range of other ligands with or without nitrogen and also be replacing NH_4^+ ion with other simple complex ions.

2. MATERIALS AND METHODS

The procedure of preparing nitrocomplexes that have the general formula mentioned above consisted in treating $CoCl_2 \cdot 6H_2O$ dissolved in distilled water with a solution which contains NH_4Cl, $NaNO_2$ and $N_4C_6H_{12}$ taken in stoichiometric ratios. The reaction took place in excess NH_4Cl and the oxidation of the reaction mixture is done by bubbling air 1.5 to 2 hours at room temperature. The product is obtained by crystallization for 12-24 hours [4,5,6,].

The $NH_4[Co(NO_2)_4(hta)_2]$ preparation

The Erdmann analogue preparation was done as flows. A sample of 91.5 g $CoCl_2 \cdot 6H_2O$ (0.4 mol) was dissolved in 200 mL distilled water which is the first solution and 100 g NH_4Cl (1.6 mol) and 112 g $N_4C_6H_{12}$ (0.8 mol), in 1050 mL distilled water is the second solution. The two solutions were mixed and a clear red with purple blue solution was obtained. The oxidation of the reactions mixture was done then allowed to crystallize for 12-24 hours. There reaction is as follows:

$4CoCl_2+8NH_4Cl+16NaNO_2+8N_4C_6H_{12}+O_2 \rightarrow 4NH_3+16NaCl+4NH_4[Co(NO_2)_4(hta)_2]+2H_2O$

The nitrocomplex was dissolved in warm water in order to recrystallize it and there was no danger of hydrolysing. In the case of Erdmann s salt recrystallization was done from a 1 M CH_3COOH solution with an efficiency of 91 %. The complex obtained has macrocrystals under the form of red bright lamellae of different sizes within regular outlines. It is partially soluble in water (0.23g/100g water at 22 °C) and it decomposes at 175 °C.

The pentanitro-and trinitrocomplexes preparation with $N_3C_6H_{12}$

Modifying the stoichiometric ratio between components (increasing $NaNO_3$ quantity and reducing the $N_4C_6H_{12}$ quantity) we obtained the pentanitrocomplex with the formula $NH_4[Co(NO_2)_4(hta)_2$. It presented macrocrystals as bright lamellae with yellow-reddish colour a little different from the one of tetranitrocomplex.

As in the case of Erdmann s salt preparation, excess of $N_4C_6H_{12}$ leads to the formation of the nonelectrolyte from with the formula $[Co(NO_2)_4(hta)_2]$ during the bubbling of air. This is a precipitate with yellow-orange colour, with microcrystals and it is hardly soluble in water.

The three nitrocomplexes, which were obtained with hexamethylenetetramine (hta), were studied using many chemical and physical-chemical methods in order to establish their composition and structure.

Cobalt was determined by complexonometrical titration using 0.01 M complexon III with murexide.

The measurement of NH_4^+ ion was done spectrometrically (λ=410 nm) using Nessler reagent>the total nitrogen was determined using the micro-Kejdahl method. The difference between the total nitrogen and the ammoniacal nitrogen represents the NO_2^- groups and complexed hta molecules.

In the table 1 are presented the data obtained through chemical analysis for the three-synthetized complexes.

3. RESULTS AND DISCUSSION

Table 1. The results of the chemical analyses

Formulae	M_{calc}	η %	Content %					
			Co		NH_4^+		N_{total}	
			Found	Calc.	Found	Calc.	Found	Calc.
$(NH_4)_2[Co(NO_2)_5(hta)]$	464.93	76.3	12.52	12.67	7.90	7.74	33.01	33.12
$NH_4[Co(NO_2)_4(hta)_2]$	536.93	91.0	10.87	10.97	3.52	3.35	33.70	33.89
$[Co(NO_2)_3(hta)_3]$	616.93	42.5	9.68	9.55	-	-	34.22	34.04

From the chemical analyses and the other physical-chemical methods which were used we proposed the following structure and the composition of the three nitrocomplexes synthetised.

$(NH_4)_2[Co(NO_2)_5(hta)]$ $NH_4[Co(NO_2)_4(hta)_2]$ $[Co(NO_2)_3(hta)_3]$

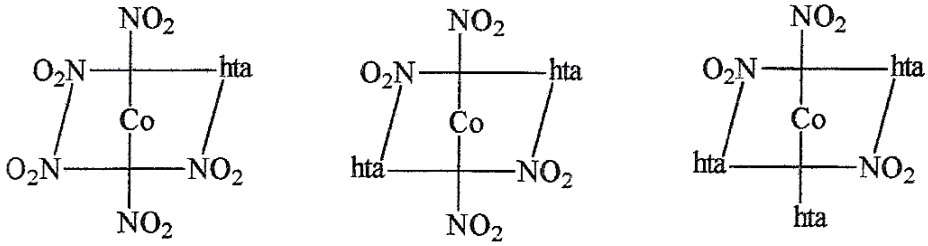

New derivatives of $NH_4[Co(NO_2)_4(hta)_2]$

The $NH_4[Co(NO_2)_4(hta)_2]$ complex is an Erdmann analogue as well as all the derivatives resulting from partial or substitution of hta groups. They contain a useful element for the plant, within the complex ion or they contain instead of the NH_4^+ cation another complexed microelement of the type $[Me(NH_3)6^{n+}$, $[Co(NO_2)_4(hta)_2]^{n-}$.

Thus, the $NH_4[Co(NO_2)_4(NH_3)(hta)_2]$ complex was studied. It was obtained by introducing into the mixture of reaction both hta (according to the stoichiometrical reaction) and NH_3 in small exces. The favourable efficiency was obtained by mixing two solutions as follows.

- the first solution was obtained by dissolving $CoCl_2 \cdot 6H_2O$ (0.4 mol) in 200 mL distilled water.

- the second solution by dissolving NH_4Cl (1.8 mol), hta (0.4 mol), $NaNO_2$(2 mol) and NH_3 25% (2 mL) in 950 mL distilled water.

Air was bubbled in the two solutions for 2 hours after mixing. The purple colour of the solution becomes red and it is turbid because the nonelectrolyte $[Co(NO_2)_4(hta)_2]$ is formed in a small quantity. It need 2-3 days for crystallizing after filtering. Crystals with bright red lamellae are obtained. The chemical and physical-chemical studies confirm the $NH_4[Co(NO_2)_4(hta)_2]$ complex composition and structure. The fact that Erdmann salt does not appear even in traces (it can be seen with naked eye), because it has dark-brown prismatic crystals, proves that hat as a ligand a higher affinity for cobalt than for NH_3.

In the same way we obtained new derivatives which contain, another ligand ion or molecule in the complex ion besides the four NO_2^- groups and one hta molecule. The formula of the new complex ion is $[Co(NO_2)_4(hta)X]^-$ where X is the ligand which is introduced by synthesis.

The table 2 presents examples of such derivatives, which are considered Erdmann analogues. In the same table are presented analogues, which are obtained by replacing the NH_4^+ cation with metallic cations such as Ag^+, Hg_2^{2+} and Tl^+. They are obtained by a simple precipitation of $[Co(NO_2)_4(hta)_2X]^-$ ion with metal salts or with ammoniac complex cations or derivatives [7,8,9].

Table 2. New analogues of $NH_4[Co(NO_2)_4(hta)_2]$

No	Complex combination	Molecular Weight Calc.	Yield %	Aspect	Analysis Co(III)	
					Calc.	Found
I	II	III	IV	V	VI	VII
1	$NH_4[Co(NO_2)_4(hta)_2SCN]$	476.73	68.20	Irregular plates Microcrystals Pink-lilas coloured	12.35	12.5
2	$NH_4[Co(NO_2)_4]_2(hta)(py)]$	480.03	71.10	Rhombic plates Macrocrystals Pink coloured	12.27	12.38

3	$Ag[Co(NO_2)_4(hta)_2(NH_3)]$	507.83	•	Plates microcrystals Dark-yellow coloured	11.60	11.32
4	$Hg[Co(NO_2)_4(hta)(NH_3]_2$	1201.04	•	Plates microcrystals Redish coloured	4.91	5.18
5	$Tl[Co(NO_2)_4(hta)(NH_3)]$	604.3	•	Plates microcrystals Dark-yelow coloured	9.75	9.60
6	$(NH_3)_2[Co(NO_2)_4(hta)(NH_3)]$	444.93	64.50	Irregular plates Microcrystals, red-brick coloured	13.24	13.11
7	$[Cu(NH_3)_4]A_2$	931.41	•	Plates microcrystals Greenish coloured	6.33	5.98
8	$[Zn(NH_3)_4]A_2$	933.23	•	Plates microcrystals Yellow-golden coloured	6.31	6.14
9	$[Co(NH_3)_4CO_3]A$	586,86	•	Plates macrocrystals Brown coloured	10.04	10.41
10	$[Co(NH_3)_4C_2O_4]A$	702.86	•	Plates macrocrystals Chocolate coloured	8.38	8.02

•-total precipating
A=$[Co(NO_2)_4(hta)(NH_3)]$

The latter compounds are hardly soluble and they have differrent colours due to the presence of the second complexed metal which could be used as a microelement for fertilizing plants [10,11].

4. CONCLUSIONS

The Erdmann complex presents properties of fertilizing plants because it contains both nitrogen under different forms and Co(III) as a microelement.But this combination has many disadvantages for use.Amog them we mention decomposing under action of light and unstable character in water solution.

The analogue obtained by us $NH_4[Co(NO_2)_4(hta)_2]$, eliminates these disadvantages because hta is tied more strogly to Co(III) and has a higher stability.The paper presents the way for obtaining and studyng the composition and structure of the above mentioned analogue and a number of other derivatives.

References

[1] G. Marcu and colab, *Chimie anorganica.*, Ed.Didactica si Pedagogica,Bucuresti (**1981)**.
[2] M. Brezeanu and P. Spacu, *Chimia CombinatiilorComplexe*,Ed. Didactica si Pedagogica,B ucuresti(**1969)**.
[3] A.G. Turner, A.F. Cliford and C.N. Rao, *Anal Chem,.* **(2012)** 1708.
[4] R. Gilchrist and B. Standarts, *J.Reasearch*, 9, **(1932**) 282.
[5] L. Winterbert, *Ann.Chem.Phys,* 7 **(1903)** 15.
[6] P. Spacu and C. Gheorghiu, *Z.Anal.Chem,* 174 **(1960**) 174.
[7] I. Ganescu and Cs. Varhely, *Polish J.Chem,* 369 **(1978)** 365.
[8] I. Ganescu, M. Mureseanu, I. Papa and A. Ganescu, *Anal.St.Univ A.I.Cuza Iasi.s.Chem.*VI, **(1998)**.
[9] J. Szako, I. Ganescu and Cs. Varhely, *J.Thermal Analysis,* 48 **(1997**) 367.
[10] N. Calu,L.burnea and S.Burnea,*Certificate of inventor, nr 84952*, Romania(1984).
[11] I. Ganescu, M. Mureseanu, A. Popescu, I. Papa and A. Ganescu, *Anal.St.Univ A.I.Cuza Iasi.s.Chem.*VII(2), **(1998)** 271.

Annals of the University of Craiova
The Chemistry Series
Volume XLV, No. 1 (2018) 46-59
homepage: chimie.ucv.ro/anale/

Analysis of the sugar profile and ascorbate content of some beverages containing orange juice

Research article

Georgeta Ciobanu, Cătălina Ionescu, Andreea Eliescu*

University of Craiova, Faculty of Sciences, Department of Chemistry, Calea București 107i, Craiova, Romania
*E-mail: geo_ciobanu20@yahoo.com

Received: 10.05.2018 / Accepted: 11.06.2018 / Published: 16.07.2018

Abstract
Eight marketed orange beverages were analyzed and compared with a freshly prepared orange juice, with regard to their soluble sugar profile, pH and ascorbic acid content. Although sugar content was largely comparable with that declared on products' labels, in many of the analyzed probes it resulted rather from added ingredients, other than the orange fruits. Fruit content of the beverages was positively correlated with ascorbate concentration and negatively correlated with its exponential decay rate. Pasteurization may contribute to ascorbate stability in the beverage not only during storage but also short time after the package's opening.

Keywords: orange beverages, sugar profile, ascorbate content and decay

1. INTRODUCTION

In living organisms, carbohydrates perform energetic, plastic and communication roles. Balanced nutrition implies an adequate intake of glucides, as most of the sugars in human food can be converted into

glucose. Disruption of glucose homeostasis can have major consequences on the body's physiology [1-3]. Simple carbohydrates can also be converted into lipids, increasing the risk of obesity and atherosclerosis [4]. Knowing the sugar content of food, in qualitative and quantitative terms, is a first step towards a rational diet for both a healthy body and for disrupted carbohydrate metabolism. In the particular case of marketed orange juices, the carbohydrate profile can be an indicator of the real fruit content and a guide to choosing the right product, beyond the information, sometimes inaccurate or ambiguous, on the product label.

We have assayed the soluble carbohydrate content of some commercial orange soft drinks, aiming to compare the obtained results with the information on the product's label, and also with the same parameters measured on a freshly prepared orange juice.

2. MATERIALS AND METHODS

2.1. Materials

Analytical grade reagents from Merck, Roth, Fluka and BioSystem were used for all solution preparation and assays. The oranges and orange juice containing soft drinks were purchased from the local stores.

2.2. Analysis methods

The main sugars in orange fruits are glucose, fructose and sucrose, their quantity and distribution depending on the analyzed source. Thus, we attempted to quantify their contents by means of simple colorimetric methods.

The total reducing sugar content was assayed in alkaline medium, with the 3,5-dinitrosalicylic acid (DNSA) as an oxidant, whose reduction to 3-amino-5-nitrosalicylic acid was monitored at 530 nm [5]. The measured absorbance values were converted into reducing carbohydrate concentrations using a calibration curve obtained with

glucose, fructose and inverted sugar as standard substances. As the obtained data for the standard curves did not show wide variations related to the tested sugar, we have used in calculations the means of the three data series (the equation of the linear regression of the data was: $A_{530}=0.1394*c_{sugar} + 0.0369$; $r^2=0.9989$); (figure 1).

Glucose was assayed at 500 nm, following the coupled enzymatic reaction of glucose oxidase (10 U mL^{-1}) and peroxidase (1 U mL^{-1}) (GOD-POD method). Quantitative results were obtained using a standard solution of 5.55 mmol L^{-1} glucose, and glucose concentration in the samples was expressed as μmol mL^{-1}.

Sucrose was first hydrolyzed to glucose and fructose by incubating volumes of 0.2 mL of the test solution with 0.2 mL of 0.3 mol L^{-1} $HClO_4$, at 90 °C for 45 min, in a water bath. The hydrolysate was neutralized with 0.3 N NaOH, and the final volume of the probe was brought to 1 mL with Tris-HCl buffer, pH 7.5. Glucose concentration and total reducing sugar content within the hydrolysate were assayed with GOD-POD reagent and DNSA reagent, respectively, as previously explained. The amount of sucrose was calculated as the difference between glucose concentration in the hydrolyzed sample (μmol mL^{-1}, *i.e.* mmol L^{-1}) and glucose concentration in the non-hydrolyzed sample. Finally, all the concentrations of soluble sugars in the analyzed samples were expressed as grams per 100 mL product.

The described methods were used for the differential assay of the sugars in orange juice containing beverage, according to the algorithm presented in figure 2. Thus, applying the DNSA method before the hydrolysis of the samples, the sum of free glucose and fructose concentrations (a + b) is obtained, while glucose concentration (a) is measured by the GOD-POD method. Consequently, fructose concentration (b) can be calculated by the difference: (a + b) - a. The DNSA method applied after probes' acidic hydrolysis will give the free glucose and free fructose concentrations (a + b), together with their quantities resulted from sucrose hydrolysis, that led to an equimolecular mixture of glucose (c) and fructose (c); that is: (a + b + 2c). Applied to the hydrolyzed probes, the GOD-POD method will measure both the free glucose in the sample and that resulted from sucrose hydrolysis (a + c).

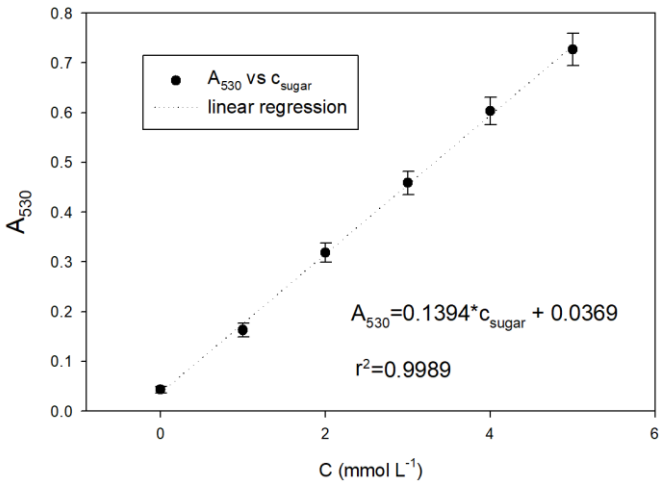

Figure 1. The standard curve for reducing sugar assay by the DNSA method

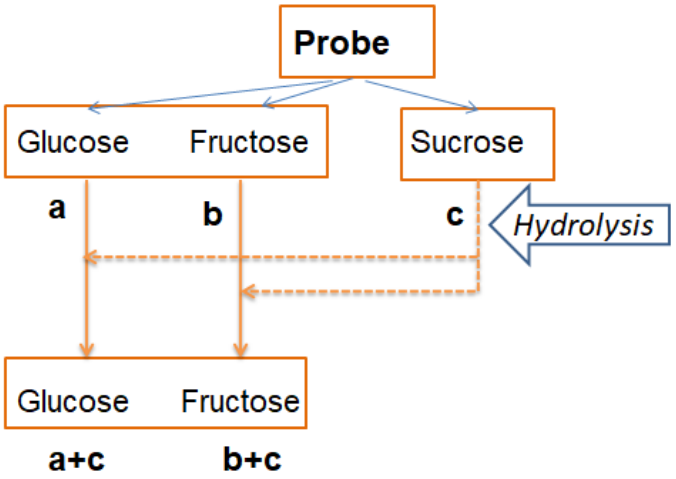

Figure 2. Schematic representation of the sequence in which sugar concentrations in the analysed samples can be determined by means of the two methods described above; *a*, *b* and *c* are the concentrations (mmol L^{-1}) of the three assayed sugars (explanations are given within the text)

Sucrose concentration of may therefore be calculated based on the results obtained with the DNSA method applied after and prior to hydrolysis (equation 1), and similarly based on the data obtained using the GOD-POD method (equation 2):

$$c = \frac{(a + b + 2c) - (a + b)}{2} \quad (1)$$

$$c = (a + c) - a \quad (2)$$

2.3. The samples and their preparation for the analyses

Eight soft drinks containing orange juices and a freshly prepared orange juice (100% fruit) were analyzed regarding to sugar content, pH and vitamin C. Certain characteristics of the analyzed soft drinks are presented in table 1. Prior to the analyses, 5 mL aliquots of the probes were centrifuged in a Sigma 2-16 K refrigerated centrifuge to remove the insoluble components, and the supernatants were decanted and assayed, as described in the previous sections. All the colorimetric measurements were performed with a Varian Cary 50 UV-Vis spectrophotometer, equipped with the CaryWin Analysis Package.

2.4. pH and ascorbic acid content measurement

The pH measurement of the beverages was done by rapid testing with pH-indicator paper Acilit®, pH 0.5-5, from Merck. Ascorbic acid content of the probes was measured using Merckoquant® Ascorbic Acid colorimetric strips (50-2000 mg L^{-1}), suitable for quickly measuring natural or added ascorbic acid in foods (fruit and vegetable juices, soft drinks). In this method, ascorbic acid reduces yellow molibdophosphoric to phosphomolybdenum blue.

The samples were put in opened glass test tubes kept at room temperature (25 °C), and ascorbic acid was measured on days 0, 1 and 4 (*i.e.* at 0; 24 and 96 hours from package opening). Values of ascorbate concentration were plotted *vs.* time, and the rate of ascorbate exponential decay (best fit) was inferred from the regression of the data, according to equation (3) [6]. In this case, parameters of the exponential

decay function were: the initial concentration of ascorbate in the sample (N_0), expressed as mg ascorbate. L^{-1}, and λ, the positive rate of the process, called exponential decay constant (for ascorbate) expressed as $days^{-1}$.

The half-life of ascorbate, expressed in *days*, in air-exposed probes was also calculated (equation 4) [7, 8].

$$N(t) = N_0^{-\lambda t} \quad (3)$$

$$t_{1/2} = \frac{\ln(2)}{\lambda} = \frac{0.693}{\lambda} \quad (4)$$

Table 1. Description and content of the analysed probes, as declared in theirs labels or technical data sheets

Probe number	Description	Content
1	100% Orange juice obtained from concentrated juice; pasteurized product.	Orange juice obtained from concentrated orange juice (97%), orange pulp (3%).
2	Orange juice rich in pulp, 100% fruit content; pasteurized product.	Orange juice (100%) obtained from concentrated orange juice.
3	Non-carbonated soft drink; pasteurized product obtained from concentrated orange juice	Water, orange juice (30%) obtained from concentrated orange juice, sucrose and/or glucose-fructose syrup, lemon juice from lemon concentrate as acidity corrector, flavor, dye: beta-carotene, vitamins: C, thiamin, niacin, B_6 and B_{12}.
4	Non-carbonated beverage with at least 15% fruit content; pasteurized product; it does not contain preservatives. Packaged in aseptic environment.	Water, sucrose, concentrated orange juice (7.5%), concentrated lemon juice (4.5%), orange pulp (3%), vitamin C, beta-carotene, natural orange flavor, natural flavors, pectin, carob gum, modified starch.
5	Non-carbonated beverage with natural orange juice	Water, sucrose, natural orange juice (min, 5%), acidifier: citric acid, flavor, stabilizers: sucrose acetate isobutyrate, carob gum, sodium starch succinate, carboxymethyl-cellulose and xanthan gum, antioxidant: ascorbic acid, dyes beta-carotenes, preservatives: sodium benzoate and potassium sorbate.

6	Carbonated beverage with orange juice, without the addition of preservatives, without artificial dyes.	Water, sucrose or glucose-fructose syrup, orange juice at least 5%, carbon dioxide, acidifying citric acid according to the recipe, natural orange flavors with other natural flavors, ascorbic acid antioxidant, beta-carotene dyes, guar gum stabilizer.
7	Carbonated soft drink with orange juice obtained from concentrate, with sugars and sweeteners.	Water, carbon dioxide, fructose-glucose syrup, orange juice concentrate (4%), acidifier: citric acid, preservative: potassium sorbate, antioxidant: ascorbic acid, sweeteners (potassium acesulfam, sucralose) stabilizer, arabic gum, dyes: beta-apo-8'-carotenal, beta-carotene.
8	Non-carbonated soft drink with orange pulp. Pasteurized product. Does not contain added preservatives.	Water, fructose-glucose syrup, orange juice concentrate (min.7%), orange pulp (at least 4%), citric acid acidifier, acidity regulator: sodium citrate, acacia gum and E445 stabilizers, ascorbic acid antioxidant, carotene dye; natural and identical natural flavors.
9	Freshly squeezed orange juice.	100% fruit

3. RESULTS AND DISCUSSION

3.1. Sugar profile of the analyzed beverages

As resulted from our data, the positive control (consisting of a freshly squeezed orange juice obtained in the laboratory just prior to the analysis), contained 53% sucrose, 24% fructose and 23% glucose (table 3), that is roughly the same as their ratio inferred from literature data [9]. Thus, we assumed the same might be the proportion of these sugars within the natural orange juices (without added carbohydrates).

Sugar content of the analyzed probes, expressed both as g per 100 mL product, and as percentage of each type (*i.e.* glucose, fructose and sucrose) from the total content, are presented in table 2 and 3,

respectively. The obtained values were compared with the ones declared on products' label.

Table 2. Sugar content of the tested soft drinks as resulted from our analyzes, *vs.* the declared nutritional data

Probe number	*Sugar content* g per 100 mL product				
	Glucose (1)	Fructose (2)	Sucrose (3)	Total (1)+(2)+(3)	Nutritional declaration (on product's label)
1	2.71	2.55	3.58	8.84	8.4
2	1.95	2.45	4.92	9.32	9.1
3	3.75	3.3	3.67	10.72	11.1
4	1.81	0.41	9.66	11.88	11.9
5	2.21	0.54	8.06	10.81	11.5
6	3.13	2.99	4.21	10.33	10.5
7	4.04	2.9	0.5	7.44	7.8
8	5.36	4.71	1.15	11.22	11.1
9	2.27	2.46	5.31	10.04	-

Our data on the total soluble sugar content of the analyzed beverages were comparable to a great extent to those inscribed on products' labels, as resulted from table 2. Considering probe 9 the positive control, as corroborated to literature data on glucidic content of orange fruits [9], we have further compared the sugar profile *(i.e.*, the type and quantity of each of the three sugars assayed) of a genuine orange juice with the results of our assays performed on the eight tested soft drinks, and also with data on theirs technical sheets. It's worth to mention that data regarding the composition of the commercialized beverages are not necessarily easy accessible or written on product's label; as a result, the choice of one or another product does not always follow a correctly informed choice.

As declared by the manufacturers (tables 1 and 3), many probes contain added sugar, in the form of sucrose or glucose-fructose syrup mainly derived from corn. One must pay some attention to corn syrup, its content and metabolism, in order to understand how healthy it is for consumption.

Table 3. Sugar profiles of the analyzed soft drinks and their sources

Probe number	Sugar content (% total)			Sources of sugars in the product (as declared by the producer)	
	Glucose	Fructose	Sucrose	Orange juice (%)	Added sugars
1	30.66	28.85	40.50	100	-
2	20.92	26.29	52.79	100	-
3	34.98	30.78	34.24	30	sucrose and/or glucose+fructose syrup
4	15.24	3.45	81.31	7.5	sucrose
5	20.44	5.00	74.56	5	sucrose
6	30.30	28.94	40.76	5	sucrose or glucose+fructose syrup
7	54.30	38.98	6.72	4	fructose+glucose syrup
8	47.77	41.98	10.25	7	fructose+glucose syrup
9	22.61	24.50	52.89	100	-

3.2. On the metabolic fate of sugars that may help an informed choice

Different sugars are differently metabolized in the human body [10]. Fructose catabolism occurs mainly in the liver and it doesn't provoke an insulin response, while glucose catabolism starts in the stomach, depending on insulin release for its complete metabolism [11, 12]. Sucrose is firstly cleaved into the constituting monosaccharides that enter the blood flow following their own course [1].

Glucose is a combustible molecule for the human body, as its oxidation by aerobic respiration releases 3.75 kcal g^{-1} [11]. Glucose catabolism takes place mainly in myocytes and adipocytes. During exercise, glucose in muscles is catabolized for energy release, following the metabolic sequence:

Glucose→*glycolysis* → *Krebs cycle*→ *mitochondrial respiration*→ CO_2 +H_2O+ ATP

Otherwise, glucose is directed to the adipocytes were it is transformed in intermediates for lipids biosynthesis [11].

Fructose metabolism occurs almost entirely in the liver, where it is used for replenishing glycogen stores and triglycerides synthesis. Excess fructose tends to be turned into lipids: stored fats promoting weight gain, and circulating ones, favoring atherosclerosis [12].

Blood glucose concentration is an important health index in humans. Its homeostasis is mainly based on the antagonistic effects of two hormones: insulin, produced by the β-cells and glucagon, synthetized by the α-cells of the endocrine pancreas. Increased blood glucose stimulates insulin secretion, leading to glucose absorption by cells and glycemia decrease. By contrast, decreased blood glucose induces glucagon synthesis and glucose release from glycogen stores [11].

So, not only the quantity of ingested sugars it is important but also their identity, as they have different fates within the body, and their excess consumption may lead to different negative consequences. The glucose+fructose syrup that often appears in the composition of commercialized beverages is a cheaper alternative for sucrose, being usually obtained from corn. The syrup may have a great fructose content and therefore a greater sweetening power (1.7×) compared to glucose. Long term consumption of corn syrup leads to abnormal growth of adipose tissue on the belly (in the abdominal area), myocardial infarction/ heart stroke and other cardiovascular diseases [13, 14].

3.3. The pH and ascorbic acid content of the probes

Besides the glucidic, energizing content, and their presumed `naturalness` (!) of the fruit-derived juices, ascorbic acid (vitamin C) is one of the ingredients that increases the nutritional value of the orange juices (and also the interest for its consuming). Orange juices are also rich in carotenoids whose roles in human health are not neglectable. Thus, there are many facts that plead for orange juice consuming but also many opened questions on both their source of ingredients and their preservation during and after processing. The ascorbic acid content of the beverages was measured immediately after package opening (and a few days thereafter). The obtained data are presented in table 4, along

with the pH values of the tested probes. As expected, the pH values of the orange beverages are in the acidic domain, with lower values for the carbonated drinks. Our data are largely consistent with those from the literature, indicatind pH values from 3,69 to 4,34 for beverages with orange. It should be noted that the acidity of the oranges (and orange juices as well) is not due only to the high content of vitamin C, as it is sometimes misinterpreted, but also to other organic acids such as citric, malic, hydroxycinnamic, folic, pantothenic. Moreover, other added ingredients in the marketed beverage may influence the product's pH.

Table 4. Data on pH values and ascorbic acid content of the probes immediately after package opening

Probe number	*pH*	$c_{ascorbic\ acid}$/ mg L^{-1}
1	4	500
2	4	500
3	4	300
4	3.5	200
5	3	100
6	3	20
7	3	50
8	4	200
9	4.2	700

As long as it comes to ascorbic acid content, one can observe that the beverages declared as 100% fruit containing (*i.e.* probes 1 and 2) had greater content of this ingredient than those with lower fruit content. Most of the probes had added ascorbic acid as antioxidant, in unmentioned quantities, and their great majority was pasteurized.

3.4. Analysis of ascorbate content decay

Most of the packaged orange beverages are obtained from concentrated orange juice. This technology involves firstly the extraction of fruit juice followed by its concentration through water evaporation, a process that also removes soluble volatiles important for the organoleptic proprieties of the product. Storage of the concentrated juice

requires its stabilization in terms of microorganisms and enzymatic activities, which is performed by thermal treatments [15]. Heating and storage also affect flavor, color and vitamin C content. Studies on thermal treatment effect on ascorbic acid content in orange juices have shown that pasteurization does not result in large ascorbate loss, although some procedures are more detrimental than other [16,17]. Non-enzymatic ascorbate degradation occurs both due to aerobic and anaerobic reactions, depending on oxygen availability and temperature. Reconstitution of the juice from concentrate may also lead to ascorbate oxidation because of the metals iron and copper in water and oxygen exposure. According to the information regarding commercial orange juice manufacture and storage, average initial content of ascorbate in these juices is 450 mg L^{-1}, and about 2.3% of it is lost by pasteurization at 103°C for 30 min [15]. However, many beverages with orange juice contain added ascorbic acid, as antioxidant.

Our data in table 5 showed that juices having the greatest fruit content (100%) also had the greatest initial ascorbate content and the lowest decay constant. Meanwhile, beverages with low fruit content (less than 10%) also had the lowest initial ascorbate content (≤100 mg L^{-1}) and the greatest decay constant.

Table 5. Parameters of the exponential decay of ascorbate content in air-exposed orange beverages, along with some potentially relevant aspects of their composition

Probe number	Parameters of ascorbate exponential decay			Probe characteristics			
	N_0/ mg L^{-1}	λ/ $days^{-1}$	$t_{1/2}$/ days	*added ascorbate*	*added preservatives*	*pasteurized*	*fruit content* /%
9	654.90	0.14	4.94	no	no	no	100
1	465.00	0.26	2.72	no	no	yes	100
2	465.00	0.26	2.72	no	no	yes	100
3	290.60	0.29	2.36	yes	no	yes	30
8	202.60	0.33	2.08	yes	no	yes	12
4	190.60	0.46	1.50	yes	no	yes	11
5	99.39	0.66	1.05	yes	yes	no	5
7	48.85	0.74	0.93	yes	yes	no	4
6	20.16	0.75	0.93	yes	no	no	5

One may observe from table 5 that ascorbate content decreased quite rapidly after opening the packages of marketed beverages, but to a less extent in case of the freshly prepared juice. One explanation could be that processed juices are missing the original biochemical means of the fruit (enzymes and certain low molecular mass antioxidants) to fight against ascorbate oxidative degradation when exposed to air. We have also observed that the unprocessed orange juice (sample 9, our positive control) was more prone to fungal contamination than the pasteurized or preservative containing beverages (samples 1-8).

Pasteurization of the beverage may contribute to ascorbate stability not only during the storage [18-21] but also for short time after opening the bottles; addition of preservatives doesn't seem to have a role against ascorbate oxidation.

4. CONCLUSION

The total sugar content of the analyzed beverages coresponded with the nutritional declarations on their labels, but scarce information is given there regarding the identity and source of these carbohydrates. Most of the analysed beverages had important quantities of added sugars, mainly as fructose-glucose syrup, whose excessive consumption is considered among the causes of certain wide spread disease, even in young people, such as obesity and diabetes. Thus, consumption of marketed orange beverages requires caution, information, and moderation. Ascorbate is an important ingredient for the nutritional value of the orange juices. Fruit content of the tested beverages was positively correlated with their ascorbate content, and values of ascorbate decay constant on the analyzed time duration varied in the opposite direction to the initial ascorbate concentration in the samples.

References

[1] J. M. Rippe and T. J. Angelopoulos, *Nutrients,* 8 **(2016)** 697.
[2] G. A. Bray and B. M. Popkin, *Diabetes care,* 37 **(2014)** 950.
[3] R. D. Feinman and E. J. Fine, *Nutr. Metab*., 10 **(2013)** 45.
[4] K. L. Stanhope, *Crit. Rev. Clin. Lab. Sci*., 53(1) **(2016)** 52.
[5] G.L. Miller, *Anal. Chem*., 31 (**1959)** 427.
[6] https://en.wikipedia.org/wiki/Exponential_decay

[7] https://en.wikipedia.org/wiki/Half-life
[8] J. Crowe and T. Bradshaw, *Chemistry for the Biosciences: The Essential Concepts*, Oxford University Press (**2014**).
[9] H. Greenfield and D.A.T. Southgate, *Food composition data: production, management and use*, 2nd ed., FAO Publishing Management Service, Roma **(2003)**.
[10] T. McKee and J.R. McKee, *Biochemistry: the molecular basis of life*, 6th ed., Oxford University Press **(2015)**.
[11] S. L. Aronoff, K. Berkowitz, B. Shreiner and L. Want, *Diabetes Spectr.*, 17 **(2004)** 183.
[12] S. Z. Sam and M. K. Empie, *Nutr. Metabol*., 9 **(2012)** 89.
[13] E.J. Schaefer, J.A. Gleason and M. L. Dansinger, *J Nutr.*, **(2009)** 1257S.
[14] S. M. Moeller, S. Adamson Fryhofer, A. J. Osbahr III and C. B. Robinowitz , *J. Am. Coll. Nutr*., 8(6) **(2009)** 619.
[15] http://orangebook.tetrapak.com
[16] S. Leizerson and E. Shimoni, *J. Agric. Food Chem*., 53 **(2005),** 4012.
[17] L. Cinquanta, D. Albanese, G. Cuccurullo and M. Di Matteo, *J. Food Sci*., 75(1), (**2010)** 46**.**
[18] M. J. Esteve and A. Frigola, *TFSB, 2* (**2008**) 128.
[19] B. R. Cvetković, M. R. Jokanović, *APTEFF*, 40 **(2009)** 1.
[20] J. Sádecká, M. Polovka,E. Kolek, E.Belajová, B. Tobolková, L. Daško and J. Durec, *JFNR*, 53 **(2014)** 371.
[21] L. Petruzzi, D. Campaniello, B. Speranza, M. R. Corbo, M. Sinigaglia and A. Bevilacqua, *Compr. Rev. Food Sci. Food Saf.*, 16 **(2017)** 668.

Annals of the University of Craiova
The Chemistry Series
Volume XLV, No. 1 (2018) 60-74
homepage: chimie.ucv.ro/anale/

Metal complexes with thioamides and thiones

An overview

Aurora Reiss, Liana Simona Sbîrnă, Irina Dăbuleanu, Maria Geanina Iovan*

University of Craiova, Faculty of Sciences, Department of Chemistry, Calea București 107i, Craiova, Romania
* E-mail: reissaurora@yahoo.com

Received: 18.05.2018 / Accepted: 28.06.2018 / Published: 16.07.2018

Abstract
The overview presents a theoretical study on the types of metal complexes with the ligands: (a) three thioamide ligands derived from dibenzofuran which are 3-thionicotinoylaminodibenzofuran (TNADBF), 3-(2'-thiothenoylamino) dibenzofuran (TTADBF) and 3-N-dibenzofurylthiourea (NDBFT); (b) three thione ligands of the type 6-aryl-3-cyano-4-trifluoromethyl-pyridine-2(1H)-thione where aryl is: C_6H_5, $C_{10}H_7$ and C_4H_3O. The study is based on the results obtained from elemental analysis, molar conductance, magnetic moment, IR and UV-vis data, molecular mass determination, NMR and EPR spectra. The thermal analysis recorded that TG, DTG and DTA experiments confirmed the assigned composition and gave information about the thermal stability of complexes in dynamic air atmosphere. In some cases a quantum-mechanical interpretation of the electronic transitions for the free and coordinated ligand was performed using EHT-MO approach in order to get more information about the atoms involved in coordination to the metallic ion. Antibacterial activity of the ligands and their complexes were investigated.

Keywords: dibenzofuran, thioamide group, metal complexes, heterocyclic thione, antibacterial activity

1. INTRODUCTION

The transformation of a carbonilic compound into a thiocarbonilic compound represented a very interesting matter for organic chemists. In 1869, Henry and Wislicenus proposed and used the first thionate agent: PS_5. Although other agents were tried (H_2S, P_4S_{10}), a considerable progress was made through the discovery of the Lawesson reagent. The advantage of this reagent is to transform a great variety of carbonilic compounds into thiocarbonilic ones, at room temperature. The disadvantage of Lawesson reagent is the difficulty to separate the product of the reaction. Thioamide is a functional group with the general structure R-CS-NR^1R^2(H) where R, R^1, R^2 are organic groups. Several research workers have used this group in the synthesis of different heterocyclic compounds such as triazoles, thiadiazoles, quinazolines, benzothiazines, benzodiazocines, benzotriazocines and benzothiadiazocines [1-5].

Thioamides (rarely, thionamides, but also known as thiourylenes) are used in many ways: for the protection of animals, as accelerators in the tire vulcanization, as inhibitors of the corrosion, for the synthesis of some heterocycles with sulphur and in electroplating industries as polyolefin stabilizers [6-10]. The fact that the drugs, which contain the thiocarbonilic group (etionamide, propionamide), have an antituberculostatic action, motivates the interest in the complex compounds with these ligands. In some cases, it was found that the antituberculosis properties could increase through the complexation with ions of the transitional metals.

The chemistry of thioamides and their derivatives continues to be of interest because their interesting structural features and also because of their biological importance. The thioamide derivatives have showed significant activities such as antitumor activity, anthelmintic activity, thyrotoxic activity, centered nervous system depressant etc [11-18]. A platinum-pyridine thione complex has been patented for clinical use in cancer treatment [19]. Fungicidal, insecticidal, and acaricidal activities have also been reported for these compounds [20].

Metallic complexes of heterocyclic thione donors are of considerable interest as a consequence of their applications, e.q. in analytical chemistry, in polymer industry and in medical-biological systems, where their bacteriostatic and cytostatic properties are useful [21-24].

Thione-thiol tautomerism (Figure 1) is a common feature among many members of this group of ligands with the thione tautomer dominant in the solid state [25].

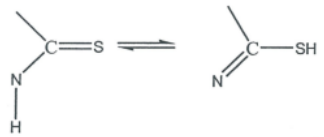

Figure 1. Thione-thiol tautomerism

However in solution, and immediately prior to complexation, the tautomeric equilibrium may be shifted by a number of factors including: the nature of the metal, the presence of base and the nature of the solvent. Deprotonation in a basic media produces the thionate moiety, which is capable of a monodentate, bidentate or bridging coordination behavior utilizing either sulfur or nitrogen atoms, or both of them, in the complexes [26].

Taking into account all these facts, in this review are presented some complex compounds of transition metallic ions with thioamides and heterocyclic thiones as ligands [27-40].

1. Metal complexes with 3-thionicotinoylaminodibenzofuran (TNADBF)

A series of transition metal complexes of Fe(II), Co(II), Ni(II), Pd(II), Pt(II), Cu(II), Zn(II), Cd(II) and Hg(II) with the ligand 3-thionicotinoylaminodibenzofuran (Figure 2) have been synthesized [27,28]. The ligand was prepared as described in literature [41].

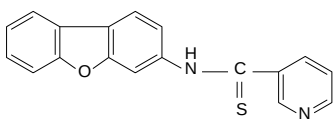

Figure 2. Structure of the ligand TNADBF

All the complexes $[MLCl_2]$, $[ML_2Cl_2]$ and $[ML_2]Cl_2$ were characterized by elemental analyses, spectroscopic methods (IR, UV-vis), conductivity and susceptibility measurements and thermal studies. In Table 1 are presented the types of complexes obtained and the structural formulation of them.

Table 1. Types of complex compounds with thioamide TNADBF(L)

Compound	Structural formulation
$MLCl_2$ a. M(II)=Ni, Pd, Pt b. M(II)=Zn, Cd, Hg	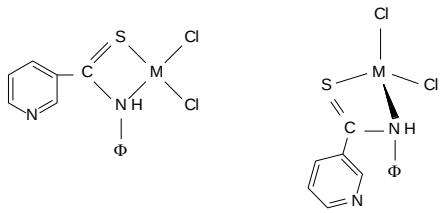 a. b.
ML_2Cl_2 M(II)=Fe, Co	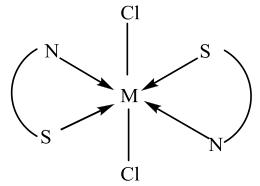
$[ML_2]Cl_2$ a. M(II)=Ni, Cu b. M(II)=Zn	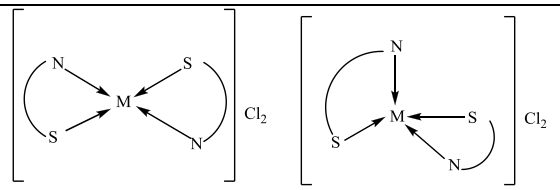 a. b.

where:

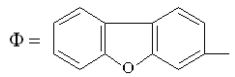

The IR spectra of the complexes were compared with those of the free ligand in order to determine the donor atoms that may be involved in coordination. In literature it is stated that thioamide forms a complex vibrational group with four characteristic bands in the 1600 - 600 cm^{-1} domain [42, 43]. Changes of the ligand spectrum upon coordination involve a significant perturbation of the characteristic four bands. So, the thioamide I, II and III bands are displaced towards higher frequencies in the complexes spectra and this suggested that nitrogen and sulphur atoms of the thioamide group are involved in coordination.

The thioamide IV band is converted from its clearly resolved components in the uncoordinated ligand into a peak with associated shoulders in the complexes. From IR spectra, it was concluded that 3-thionicotinoylaminodibenzofuran behaves as a bidentate ligand in all the complexes and that the coordination takes place at the sulphur and nitrogen atoms of the thioamide group.

Evidence for the bonding mode of the ligand is provided also by the ^{1}H-and ^{13}C-NMR spectra of the ligand and of the diamagnetic $[ZnL_2]Cl_2$ complex (Table 2 and Figure 3) which were recorded in the same solvent $CDCl_3$.

Table 2. Major NMR signals for thioamide TNADBF (L) and $[ZnL_2]Cl_2$

Compound	δ_{NH} (ppm)	$\delta_{C=S}$ (ppm)	δ_{NH2} (ppm)
L	12.2	195.1	-
$[ZnL_2]Cl_2$	11.5	190.1	-

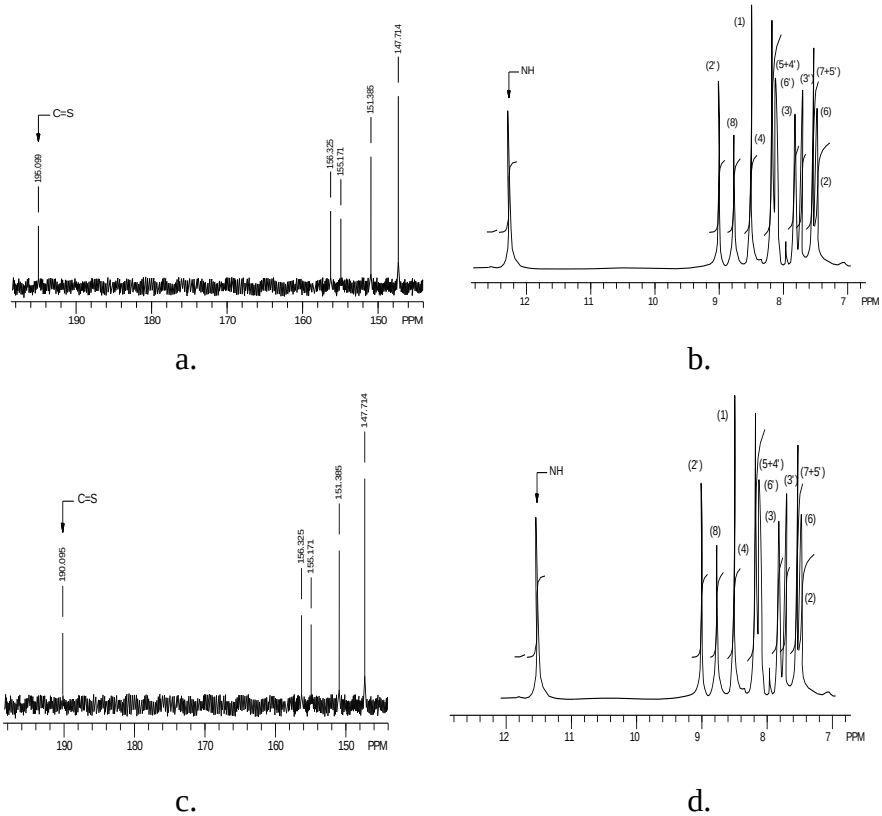

Figure 3. ^{13}C and ^{1}H-NMR spectra of the ligand TNADBF (a, b) and Zn(II) complex (c, d)

A quantum-mechanical interpretation of the electronic transitions for the free and coordinated ligand in the $[NiL_2]Cl_2$ complex has been performed using EHT-MO approach given by the ICONC program [44] in order to get more information about the atoms involved in coordination to the metallic ion. According to all these information, it was proposed an octahedral geometry for $[FeL_2Cl_2]$ and $[CoL_2Cl_2]$ complexes, a square-planar geometry for $[NiL_2]Cl_2$ and $[CuL_2]Cl_2$ complexes and a tetrahedral geometry for $[ZnL_2]Cl_2$ complex. The metal complex structures are given in table 1.

Antibacterial activity of the ligand TNADBF(L) and its complexes were studied against selected bacteria E. coli, S. aureus and P. aeruginosa. It has been found that all the complexes are antimicrobially active and show higher activity than the free ligand. The biological activity of the complexes follow the order, Fe(II)>Co(II)=Ni(II)=Cu(II)>Zn(II).

A possible explanation for the increased activity upon chelation is that in the chelated complex, the positive charge of the metal ion is partially shared with the donor atoms of the ligand and a π- electron delocalization occurs over the whole chelate ring, increasing in this way the lipophilic character of the metal chelate and favoring its permeation through the lipoid layers of the bacterial membranes and blocking the metal binding sites in the enzymes or microorganism. Other factors such as solubility, conductivity and dipole moment (influenced by the presence of metal ions) may also be the possible reasons for increasing this activity [45, 46].

2. Complex compounds with 3-(2′-tiotenoilamino)dibenzofuran (TTADBF)

A series of transition metal complexes of Ni(II), Pd(II), Pt(II), Au(III), Zn(II), Cd(II), Hg(II) and Cu(I) (Table 3) with the ligand 3-(2′-tiotenoilamino)dibenzofuran (Figure 4) have been synthesized [29, 30, 33]. The ligand was prepared as described in literature [41].

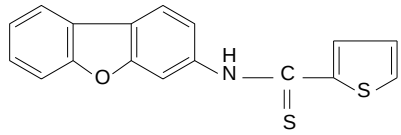

Figure 4. Structure of the ligand TTADBF

The metal complexes are powders or microcrystalline plates with medium stability and reduced solubility in common organic and inorganic solvents such as: methanol, ethanol, dioxane, benzene, rthyl ether and diluted hydrochloric, nitric, sulphuric acids, respectively, and with melting points higher than the pure thioamide. In Table 3 are presented the types of complexes obtained and the structural formulation of them.

Table 3. Types of complex compounds with TTADBF

Compound	Structural formulation
$MLCl_2$ a.M=Ni, Pd, Pt b.M=Zn, Cd, Hg	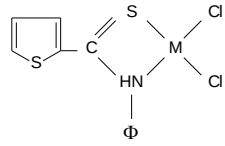 a. 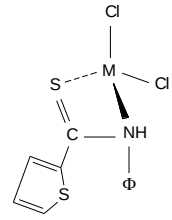 b.
$[AuLCl_2]Cl$	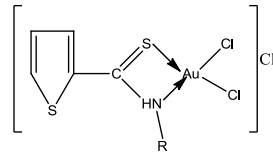
$(CuCl)_2L_2$	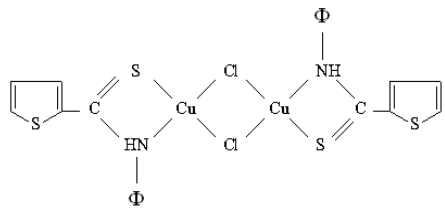 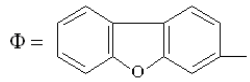

All the complexes were characterized by elemental analyses, spectroscopic methods (IR, UV-vis), conductivity and susceptibility measurements. The studies on the Cu(I) complex were completed by molecular mass measurements (Rast method). The results prove that the complex compound is in dimeric state (molecular weight calcd. 816.08, found 802.76). Evidence for the bonding mode of the ligand is provided also by the ^{1}H-and ^{13}C-NMR spectra of the ligand TTADBF and of the diamagnetic $ZnLCl_2$ complex (Figure 5) which were recorded in the same solvent $CDCl_3$. The ^{13}C-NMR spectrum of the free ligand TTADBF presents a peack at δ187,1 ppm which it is shifted at δ185,3 ppm in Zn(II) complex spectrum indicates that sulphur atom is coordinated to metallic ion. The ^{1}H-NMR spectrum of free ligand presents a singlet at δ11,8 ppm assigned to imido (–NH–) group which is shifted with 0,8 ppm in Zn(II) complex spectrum. This change indicates the coordination of nitrogen atom to metallic ion.

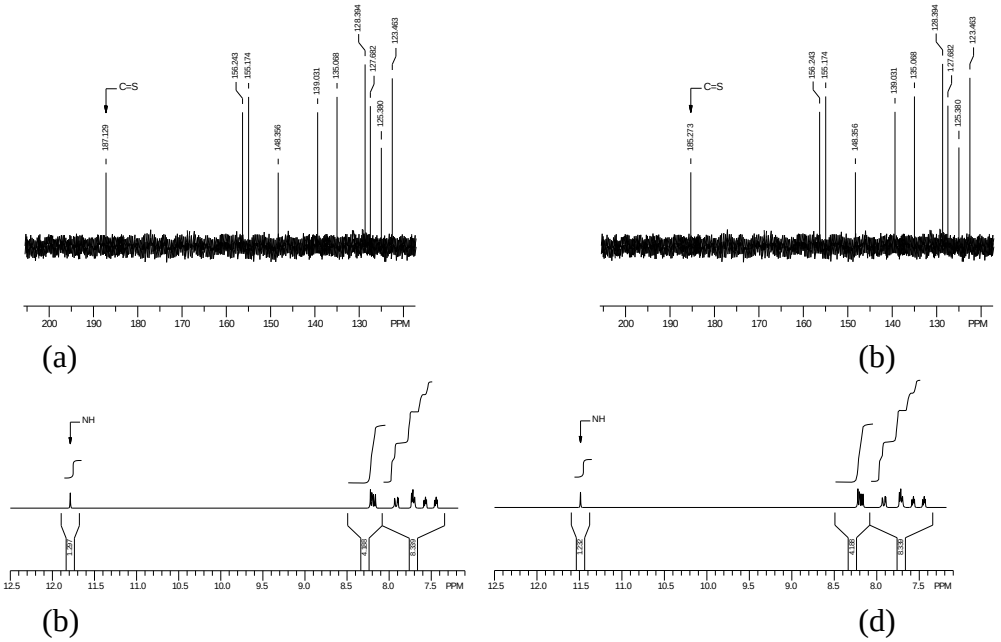

Figure 5. ^{13}C and ^{1}H-NMR spectra of the ligand TTADBF (a, c) and Zn(II) complex (b, d)

3. Complex compounds with 3-N-dibenzofuryl-thiourea (NDBFT)

A series of transition metal complexes of Fe(II), Co(II), Ni(II), Cu(I), Zn(II), Cd(II), Pd(II) and Pt(II) (Table 4) with the ligand 3-N-dibenzofuryl-thiourea (Figure 6) have been synthesized [31,32,34]. The ligand was prepared as described in literature [47].

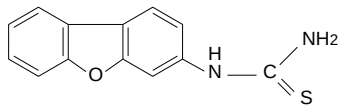

Figure 6. Structure of the ligand NDBFT

The complexes were characterized by elemental analyses, IR, UV-vis and NMR spectra, conductivity and susceptibility measurements, thermal studies and molecular mass determination. In Table 4 are presented the types of complexes obtained and the structural formulation of them.

Table 4. Types of complex compounds with NDBFT(L)

Compound	Structural formulation
$MLCl_2$ a. M=Co, Ni, Pd, Pt b. M=Zn, Cd	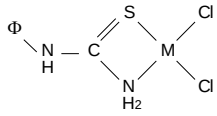 a. 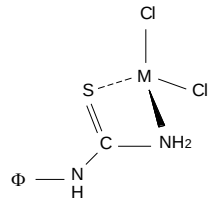 b.
ML_2Cl_2 where M=Fe	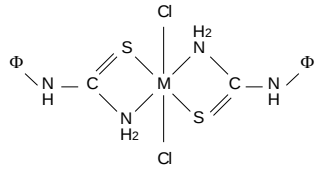
$(CuCl)_2L_2$	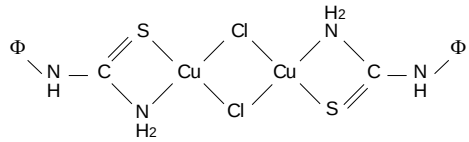
where:	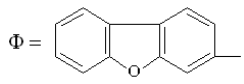

The thioamide ligand NDBFT which contains -NH- and -NH_2 groups and it appears the question: which nitrogen atom participates in the chemical bond? To obtain supplementary information about the bonding mode of ligand in complexes, the ^{1}H-and ^{13}C-NMR spectra of ligand and Zn(II) complexe were performed. The results are presented in table 5 and Figure 7. The signal due to the carbon atom of the C=S group shifts towards high fields in the spectra of the complex because of complexation to the metallic ion. The signal of –NH– group in the ^{1}H-NMR spectrum of NDBFT is not shifted after complexation and this fact means that the nitrogen atom does not participate in the bonding process. But, the signal of -NH_2 group, which appear at 7.1 ppm in the spectrum of the ligand, after complexation is shift towards high fields (6.7 ppm) because of the coordination of the nitrogen atom. In conclusion, the chemical bond in complexes with the thioamide NDBFT implies the participation of the sulphur atom of the C=S group and the nitrogen atom of the –NH_2 group.

Table 5. Major NMR signals for thioamide NDBFT(L) and Zn(II) complex

Compound	δ_{NH} (ppm)	$\delta_{C=S}$ (ppm)	δ_{NH2} (ppm)
NDBFT (L)	9.4	183.7	7.1
$ZnLCl_2$	9.4	180.7	6.7

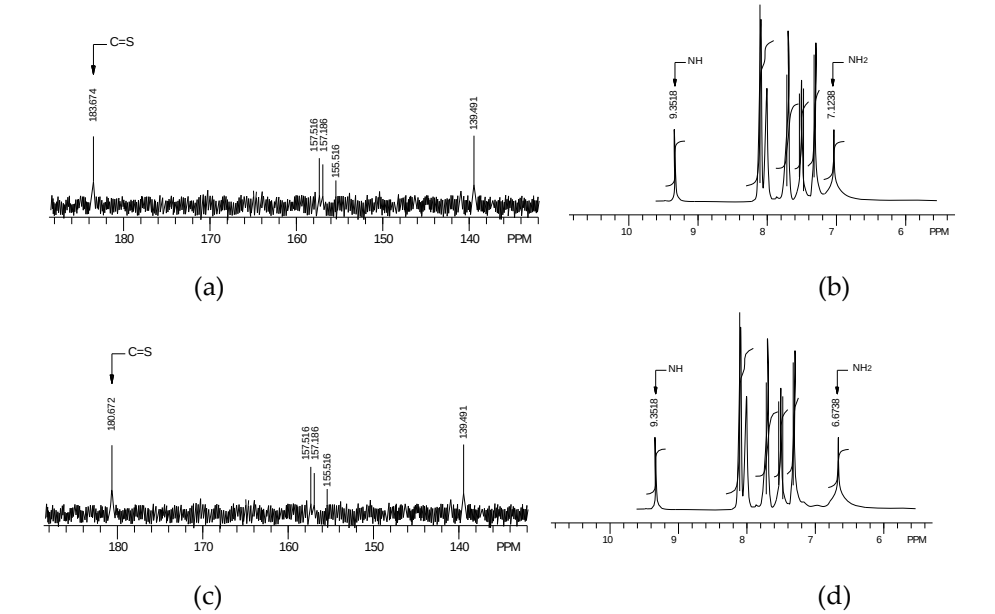

Figure 7. ^{13}C and ^{1}H-NMR spectra of the ligand NDBFT(a, b) and Zn(II) complex (c, d)

The thioamides NDBFT and TTADBF and their complexes with Ni(II), Pd(II) and Pt(II) were tested for antibacterial activity using the diffusion method [11,12] against S. aureus, P. vulgaris, E coli, B piocianic, B subtilis. The same quantity of substance (1 mg) was used and after 18 hours of incubation, the diameter of the inhibition area was measured. The results which express the diameter of the inhibition area (Φ) regarding the growth of the bacteria due to the tested substances, are presented in table 6.

Table 6. The antibacterial activity of NDBFT and TTADBF and their complexes

Compound	Bacteria / Φ (mm)				
	St. aureus	Pt. vulgaris	E. coli	B. piocianic	B. subtilis
NDBFT	20	19	21	22	23
$Ni(NDBFT)_2Cl_2$	15	15	14	13	14
$Pd(NDBFT)Cl_2$	16	17	17,5	17,5	18
$Pt(NDBFT)Cl_2$	18	19	19,5	20	18,5
TTADBF	25	27	29	30	32
$Ni(TTADBF)Cl_2$	15	16	16	17	18
$Pd(TTADBF)Cl_2$	18	18,5	19	20	19
$Pt(TTADBF)Cl_2$	20	19	20	22	21

The values revealed that NDBFT and TTADBF thioamides are more active than the corresponding complexes. The decrease of the antibacterial activity is caused by the coordination of the sulphur and nitrogen donor atoms to the metallic ions. The order of the antibacterial activity for ligands and for complexes is the following: TTADBF > NDBFT; Pt > Pd > Ni.

TTADBF presents the most ample antibacterial activity probably because of the presence of furan heterocycle in its molecule. The complexes with the same ligand, which present differences regarding the diameter of the inhibition area, prove that the biological action depends not only on the characteristic of the tested molecule, but also on the biological substrate.

4. Metal complexes with 6-aryl-3-cyano-4-trifluoromethyl-pyridine-2(1H)-thione

The synthesis and characterisation of the products obtained by the reaction of 6-aryl-3-cyano-4-trifluoromethyl-pyridine-2(1H)-thione where aryl is: C_6H_5, $C_{10}H_7$ and C_4H_3O, with Co(II), Ni(II), Cu(II), Zn(II), Pd(II) and Pt(II) were reported [35-40]. The ligands were prepared as described in literature [7, 48].

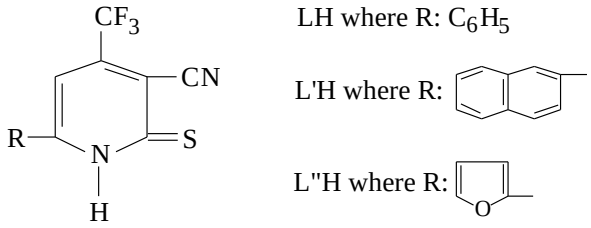

Figure 8. Structure of the ligand 6-aryl-3-cyano-4-trifluoromethyl-pyridine-2(1H)-thione

The elemental analysis data for C, H, N and S show that the complexes prepared are of the type: $[M(LH)_2(OAc)_2]$, $[M(L'H)_2(OAc)_2]$, $[M(L''H)_2(OAc)_2]$, where M(II)=Co, Ni and Zn. Cu(II) acetate reacted with 6-aryl-3-cyano-4-trifluoromethyl-pyridine-2(1H)-thione where aryl is: C_6H_5, $C_{10}H_7$ and C_4H_3O and gave extremely insoluble species containing no acetate; it presumably contains ionized pyridine-2-thione. They had the stoichiometry $(CuL)_n$, $(CuL')_n$, $(CuL'')_n$ and they were not studied further; $[Pd(LH)_2Cl_2]$, $[Pd(L'H)_2Cl_2]$, $[Pd(L''H)_2Cl_2]$, $[Pt(LH)_2Cl_2]$, $[Pt(L'H)_2Cl_2]$, $[Pt(L''H)_2Cl_2]$.

IR spectra of the complexes and the thiones were analysed and the conclusions are as follows: slight perturbation to the thioamide II(ν(C-N)+δ(C-H)+ν(C=S)) and III(ν(C-N)+ν(C=S)) bands and major perturbation to the thioamide IV (ν_s(C=S)+ν_{as}(C=S)) band (800-500 cm^{-1}) thus confirming that only sulphur atom participates in bonding to the metallic ion.

The coordination of heterocyclic thiones through the sulphur atom of the thione group is deduced from ^{13}C-NMR spectra, when, the signal due to the carbon atom of the C=S group shifts towards high fields because of the complexation [49]. In this case when the sulphur is

coordinated, the signal is observed at lower fields than those of the free ligands. This change is accounted for as follows: CF_3 and CN are groups intensely attracting electrons and they reduce the order of the chemical bond in the thione group C=S and, by complexation, the order of this chemical bond increases. Consequently, the signal of the carbon atom from C=S group shifts towards a lower field [35].

A quantum-mechanical interpretation of the electronic transitions for the free L'H thione and coordinated L'H thione ligand in the Ni(II) and Co(II) complexes has been performed using EHT-MO approach in order to get more information about the atoms involved in coordination to the metallic ion [38].

On the results obtained from UV-vis spectra and the values of magnetic moments, the geometries proposed for the complexes with the heterocyclic thiones are: square-planar for Ni(II), Pd(II) and Pt(II) complexes and tetrahedric for Co(II) and Zn(II) complexes (Figure 9).

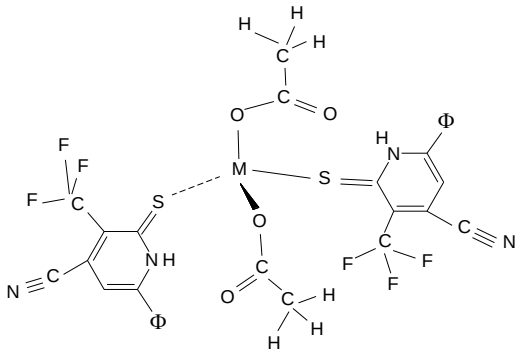

Figure 9. Proposed structure for Co(II) and Zn(II) complexes

The thiones and their metal complexes were tested for antibacterial activity by using the dilution technique [50, 51] at concentrations of 300, 200 and 100 μg mL^{-1} against *E. coli* and *S. aureus*. The results reveal that metal complexes are more active than the free thiones.

CONCLUSION

The present overview presents types of complex compounds of metal ions with the thioamides TTADBF, TNADBF and NDBFT and with 6-aryl-3-cyano-4-trifluoromethyl-pyridine-2(1H)-thione where aryl is: C_6H_5, $C_{10}H_7$ and C_4H_3O. In all obtained complexes, the thioamides participate in the coordination with both sulphur and nitrogen atoms of the thioamide group. In case of complexes with thiones, the ligands participate in the coordination to the central metallic ion only with sulphur atom of the thione group.

Bacteriological data revealed that metal complexes have appreciably lower diameter of the inhibition area than thioamides or thiones.

REFERENCES

[1] P. Wipf and V. Venkatraman, *J. Org. Chem.*, 61 (**1996**) 804.
[2] O. A. Attanasi, S. Berretta, L. D. Crescentini, G. Favi, F. Filippone, G. Giorgi, S. Lillini, F. Mantellini, *Tetrahedron Lett.*, 48 (**2007**) 244.
[3] S. P. McManus, K.Y. Lee and C. U. Pittman, *J. Org. Chem.*, 39 (**1974**) 304.
[4] T.S. Jagodziñski, *Chem. Rev*. 103 (**2003**) 197.
[5] H. Prokopcová and C.O. Kappe, *J. Org. Chem.*,72 (**2007**) 444.
[6] S. Yadav, O. P. Pandey and S. K. Sengupta, *Transit. Metal Chem.*, 20 (**1995**) 107.
[7] R. M. Oik, B. Oik,W. Dietzsch, R. Kirmse and E. Hoyer, *Coordin. Chem. Rev.*, 117 (**1992**) 99.
[8] P. J. Blower and J. R. Dilworth, *Coordin. Chem. Rev.***76**, 121, (**1987**).
[9] K.A. Petrov and L.N. Andreev, *Usp. Khim.*, 38 (**1969**) 41.
[10] T. A. Vannelli, A. Dykman and P. R. O. de Montellano, *J. Biol. Chem.*, 277 (**2002**) 128.
[11] X. Hanoulle, J.M. Wieruszeski, P. Rousselot-Pailley, I. Landrieu, A. R. Baulard and G. Lippens, *Biochem. Biophys. Res. Commun.*, 331 (**2005**) 452.
[12] C. Vilchèze, T. R. Weisbrod, B. Chen, L. Kremer, M. H. Hazbón, F. Wang, D. Alland, J. C. Sacchettini and W. R. Jacobs, *Antimicrob. Agents Chemother.* , 49 (**2005**) 708.
[13] K. L. Yu, A. F. Torri, G. Luo, C. Cianci,K. Grant-Young, S. Danetz, L. Tiley, M. Krystal and N. A. Meanwell, *Bioorg. Med.Chem. Lett.*, 12 (**2002**) 3379.
[14] Y. Hitotsuyanagi, T. Hasuda, Y. Matsumoto, K. Yamaguchi, H. Itokawa and K. Takeya, *Chem. Commun.*, (**2000**) 1633.
[15] 15.H. D. Schell, M. A. Mateescu, T. Benția and A. Jifcu, *Anal. Lett.*, 14 (**1981)** 1501.
[16] Y. Nakagawa, K. Irie, H. Ohigashi, H. Hayashi and P. A. Wender, *Bioorg. Med. Chem. Lett.*, 10 (**2000**) 2087.
[17] M. P. Wentland, X. Sun, Y. Bu, R. Lou, D. J. Cohen and J. M. Bidlack, *Bioorg. Med. Chem. Lett.*, 15 (**2005**) 257.
[18] 18.Q. L. Wei, S. S. Zhang, J. Gao, W. H. Li, L. Z. Xu and G. Z.Yu, *Bioorg. Med. Chem.*, 14 (2006) 7146.

[19] E. S. Raper, *Coord. Chem. Rev*. 153 (**1996**) 199.
[20] S. Sinha, A. K. Srivastava, C. M. Tripathi, O. P. Pandey and S. K. Sengupta, *Bioinorg. Chem. Appl.*, 18, (**2007**) 879.
[21] N. A. Bell, S. J. Coles, C. P. Constable, D. E. Hibbs, M. B. Hursthouse, R. Mansour and E. S. Raper, C. Sammon, *Inorg. Chim. Acta*, 323 (**2001**) 69.
[22] E.S. Raper, *Coord*. *Chem. Rev*., 129 (**1994**) 91.
[23] J.P. Street, K.I. Skorey, R.S. Brown and R.G. Ball, *J. Am. Chem. Soc.*, 107 (**1985**) 7669.
[24] E. W. Ainscough, E. N. Baker, A. G. Bingham and A. M. Brooks, *J. Chem. Soc. Dalton Trans*., (**1989**) 39.
[25] C. Preti, G. Tosi, *Can. J. Chem*., 54 (**1976**) 1558.
[26] N. A. Bell, W. Clegg, S. J. Coles, C. P. Constable, R. W. Harrington, M. B. Hursthouse, M. E. Light, E. S. Raper, C. Sammon and M. R. Walker, *Inorg. Chim. Acta*, 357 (**2004**) 2091.
[27] A. Kriza, A. Reiss, V. Mureșan and S. Florea, *J. Indian Chem. Soc*., 76 (**1999**) 406.
[28] A. Reiss and M. Mureșeanu, *J. Chil. Chem. Soc*., 57 (**2012**) 1199.
[29] V. Mureșan, S. Florea, A. Reiss and L. S. Mureșan, *Polish J. Chem*., 69 (**1995**) 385.
[30] V. Mureșan, A. Reiss, L. S. Sbîrnă, N. Mureșan and S. Florea, *Polish J. Chem*., 72 (**1998**) 2034.
[31] A. Kriza, A. Reiss, Ş. Blejoiu, L. Brujan and N. Stănică, *J. Indian Chem. Soc.*, 77 (**2000**) 488.
[32] A. Kriza, A. Reiss and N. Stănică, *Rev. Roum. Chimie,* 46 (**2001**) 503.
[33] V. Mureşan, N. Mureşan and A. Reiss, *Polish J. Chem.*, 67 (**1993**) 2113.
[34] V. Mureşan, L. Mureşan and A. Reiss, N. Mureşan, *Rev. Roum. Chimie*, 42 (**1997**) 193.
[35] A. Reiss, S. Florea and W. D. Rudorf, *Polish J. Chem.*, 74, (**2000**), 589.
[36] A. Kriza, A. Reiss, S. Florea and A. Meghea, *Polish J. Chem*., 74 (**2000**) 585.
[37] A. Reiss, W. D. Rudorf, Ş. Blejoiu and R. Deva, *J. Indian Chem. Soc.*, 77 (**2000**) 438.
[38] A. Reiss, C. Lepădatu and A. Kriza, *Rev. Chim.*, *57* (**2006**) 245.
[39] A. Reiss, M. Mureşeanu and N. Mureşan, *Rev. Chim.*, 59 *(***2008**) 3.
[40] A. Reiss and I. Nicolaescu, *Annals of the University of Craiova*, The Chemistry Series, XXXVII (**2008)** 26.
[41] S. Florea, *Rev. Roum. Chim.*, 39 (**1994**) 1138.
[42] K. A. Jensen and P. H. Nielsen, *Acta Chem. Scand.*, 20 (**1996**) 597.
[43] H. O. Desseyn and M. A. Herman, *Spectrochim. Acta*, 23A (**1967**) 2457.
[44] G. Calzaferri and M. Brände, *QPCE Bulletin* 12 (**1992**) 73.
[45] B.G.Tweedy, Phytopathology, 55 (**1964**) 910.
[46] A. Kleinzeller, Physiology, 12 (1997) 49.
[47] V. Cesrinsteins and G. Cerna, *Latviajas PSR Zinatum Akad. Vestis. Khim*., 247 (**1962**) 7.
[48] L.A.Rodinovskaya, Yu.A.Sharanin, V.P.Litvinov, A.M.Shestopalov, V.K. Promonenkov, B.M.Zolotarev and V.Yu. Mortikov, *Zh. Org. Khim*., 21 (**1985**) 2439.
[49] E.S. Raper, *Coord*. *Chem. Rev*., 61 (**1985**) 115.
[50] E. Duca, M. Duca, *Microbiologie medicală*, Did. și Ped. Ed., (**1979**).
[51] V. Zotta, *Chimie farmaceutică*, Med. Ed., (**1985**).

Annals of the University of Craiova
The Chemistry Series
Volume XLV, No. 1 (2018) 75-88
homepage: chimie.ucv.ro/anale/

New electrodes based on cerium modified mesoporous TiO_2 for simultaneous treatment of waste water and electricity production

Short Communication

Valentina Chivu[1], TeodorDiaconu[2], Ion Trandafir[1], Nicoleta Cioateră[1], Marcel Ionică[3], Mihaela Mureșeanu[1]*

[1] University of Craiova, Faculty of Sciences, Department of Chemistry, Calea București 107i, Craiova, Romania
[2] "Ilie Murgulescu" Institute of Physical Chemistry, Romanian Academy, Splaiul Independentei 202, Bucharest, Romania
[3] S.C.IPA S.A, CIFATT Craiova, Mihai Viteazul 1, Craiova, Romania
* E-mail: cvu_valentina@yahoo.com

Received: 08.06.2018 / Accepted: 09.07.2018 / Published: 16.07.2018

Abstract
Photo-catalytic fuel cells (PFC) is a promising technology, environmental friendly, for waste water treatment and for the simultaneous production of electricity. In this work, a novel photo anode is proposed to enhance photo electrochemical and photocatalytic activities. This one consist on a thin layer of a mesoporous TiO_2 oxide prepared by sol-gel process, in the presence of nonionic structure directing agents and modified by direct synthesis with 5% CeO_2, deposited by spin coating technique onto FTO conductive glass. The photoactive materials were characterized by X-ray diffraction (XRD), nitrogen adsorption–desorption, SEM microscopy, UV-VIS spectroscopy, and photo electrochemical analysis. The effect of the titania mesoporous structure and ceria doping on the performance of the proposed photoanode was also investigated both for phenol degradation and for electricity generation. Based on the obtained results this new photoanode could be considered for the construction of an efficient photo electrochemical system.

Keywords: photo-catalytic fuel cell, mesoporous titania, phenol degradation

1. INTRODUCTION

Photo-catalytic fuel cell (PFC) are environment-friendly technologies for the treatment of wastewater and simultaneous generation of electricity. Photocatalytic oxidation has been tested as an efficient method for degradation of various types of hazardous and persistent pollutants, and TiO_2 is the most widely used catalyst in photocatalytic processes [1,2]. TiO_2 crystallized as anatase with broad band turned out to be the most efficient material for photo anode construction due to low price, good stability, commercial availability, optical compatibility, electronic properties and non-toxicity [3]. The main problem with TiO_2 is its light absorption capacity (it can absorb radiation only from the UV region of the spectrum) and the low mobility of the electrons. By doping with the corresponding cations / anions alters the band gap and thus can change its electrical and optical properties. Cerium doped titanium dioxide has confirmed its increased efficiency by introducing impurity levels below the conduction band and reducing the energy of the optical band respectively [4]. Doping of titania with ceria has received a great interest due to the optical and catalytic properties of ceria that improved the photocatalytic activity, namely presence of the redox Ce^{3+}/Ce^{4+}couple, high thermal stability, high electrical conductivity and large oxygen storage capacity [5,6].

In this paper, a novel photoanode based on mesoporous TiO_2 modified by direct synthesis with 5% CeO_2 is proposed to enhance photo electrochemical and photocatalytic activities. The effect of the titania mesoporous structure and ceria doping on the performance of the proposed photo anode was also investigated both for phenol degradation and for electricity generation. Based on the obtained results this new photoanode could be considered for the construction of an efficient photo electrochemical system.

2. MATERIALS AND METHODS

2.1. Materials

All chemicals were commercially purchased and used without further purification. The Pluronic P123 triblock copolymer surfactant, propyl alcohol, HCl, titanium butoxide (TBOT) and $Ce(NO_3)_3 \cdot 6H_2O$ were used for the synthesis of the photoanode materials.

2.2. Synthesis of materials

The synthesis of the mesoporous TiO_2 or TiO_2 modified with CeO_2 has been achieved by the evaporation-induced self-assembled (EISA) method, using as precursors titanium butoxide for titania, cerium nitrate for ceria and the sol-gel process. In the first step, the surfactant (Pluronic P123 triblock copolymer) was dispersed in propyl alcohol under stirring. HCl was introduced into the mixture and stirring was continued for 3 hours and thereafter titanium alkoxide (TBOT) was added dropwise. For the ceria modified sample, the calculated amount of cerium nitrate was added together with TBOT in order to obtain 5% weight of CeO_2 in the final product. After another 2 hours of stirring, the obtained sol was placed in a Petri dish and left overnight at 35-40°C. The obtained gel was detached and dried at 80°C overnight. The thus obtained solid was calcined at 400°C for 8 hours (the heating rate was 2°C min^{-1}). The ultimate molar ratio was as follows: Ti: Ce: P123: HCl: H_2O: PrOH=1: 0.0245: 0.02: 1.18: 11: 33.4. The samples were denoted TGP (mesoporous TiO_2) and TGP5C (TiO_2 with 5%CeO_2).

The semiconductor oxide film was deposited on conductive glass with Fluorinated Tin Oxide (FTO) conducting layer by sol-gel method. In the first step, the support was cleaned by ultra-sonication in an acetone / ethanol bath, washed with water and a mixture of isopropyl alcohol/water and dried thereafter in a desiccator. The oxide films were deposited on the cleaned support by spin coating using the gel of titanium oxide obtained in the Petri dish after 2 hours at 40 °C. After deposition, the films were dried at 80 °C for 4 hours and calcined at 400 °C for 4 hours. Another layer was thereafter deposited. Thus, films

of 1, 2 and 3 layers were obtained. After each layer deposition, electrodes were dried and calcined. Thus, TiO_2 and CeO_2 (5%)-TiO_2 films were obtained.

2.3. Material characterization

The structure of the samples was examined at small and wide angles on a Rigaku Ultima IV diffractometer using Cu Kα (λ = 0.15406 nm) radiation. The textural properties and porosity of the materials were studied by adsorption-desorption of nitrogen with a Micromeritics ASAP 2020 automated gas sorption system. Before measurements, the samples were outgassed at 573 K for 6 h. The chemical microanalysis by scanning electron microscopy (SEM) was performed on a FEI Quanta 3D FEG scanning microscope. Several images at various positions for each sample were obtained to gain better knowledge of the surface morphology. UV–Vis spectra were recorded on JASCO V-570 UV-VIS spectrophotometer.

2.4. Photo electrochemical characterization

Electrochemical characterization of the mesoporous photocatalyst samples obtained as powder was performed using a Zahner IM6eX electrochemical station and a potentiostat/galvanostat PG581 in a three electrodes photoelectrochemical system that contains: the Ag/AgCl as the reference electrode, the Pt as auxiliary electrode and the analyzed photo anode as the working electrode (Figure 1). The working electrode was prepared as follows: 5 mg of TGP or TGP5C photo catalysts was suspended in a mixture of 400 μL isopropanol and 10 μL Nafion solution and was ultra-sonicated for 30 min. The suspension was spread onto the cleaned FTO substrate (ultra-sonication sequentially in acetone, isopropanol and ethanol baths for 15 min each), dried at 65 ^{0}C for 30 min and left to cool naturally. The support electrolyte was 0.2M Na_2SO_4. Linear sweep voltammetry (LSV) was used to measure the photo-currents, in a potential range of -1.0V to +1.0V vs. Ag/AgCl at a 10 mV/s sweeping rate with or without illumination. The Nyquist plots were registered to evaluate the changes of the charge transfer resistance with

or without illumination, at 0V towards the reference electrode in the 2.5 MHz-0.1 Hz frequency range.

Figure 1. Photoelectrochemical cell with three electrodes

The photo electrochemical characterization of the photo anodes obtained by sol-gel process and spin-coating technique, was done in the same photo electrochemical cell, with or without illumination and using as support electrolyte either 0.2M Na_2SO_4 or 0.2M Na_2SO_4+0.2M CH_3COOH (pH 4.6). A 55W Xenon lamp was uses for photo anode illumination at a 5 cm distance from the cell in all photo electrochemical experiments.

2.5. Photocatalytic activity

The photocatalytic activity of TGP and TGP5C samples was measured in the phenol photo degradation reaction in aqueous solution. The experiments were performed in a stationary quartz reactor of 6 mL under illumination for 30 min, with a 55W Xenon lamp. The initial concentration of phenol was 5 ppm and the amount of the catalyst was 0.03 g. This solution was magnetically stirred in dark for about 30 min prior to irradiation in order to reach the adsorption equilibrium and so the loss of compound due to adsorption could be considered. All experiments were conducted at room temperature and before analysis the samples were filtered through a 0.45 μm Millipore membrane filter.

The separation and quantification of the reaction products were done by using a Surveyor Thermo Electron HPLC system (Thermo Scientific) as previously described [5].

The photocatalytic activity of the photo anodes based on the new synthesized materials was tested in the same photo electrochemical cell used for photo electrochemical characterization with 50 mL of a 5ppm phenol solution, under illumination with a 55W Xenon lamp for 30 minutes. The phenol degradation was appreciated based on HPLC analysis previously described [5].

3. RESULTS AND DISCUSSION

3.1. Mesoporous TiO2 and CeO2-TiO2 powders characterization

X-ray diffraction (XRD)

The X-ray diffraction patterns of un-modified and ceria modified TiO_2 samples revealed only the anatase phase (Figure 2) after their heat treatment carried out in air at 400°C, However, peaks attributed to cerium oxides have not been highlighted. This indicates a good dispersion of ceria in the network and its undetectable content in the sample obtained at this calcination temperature.

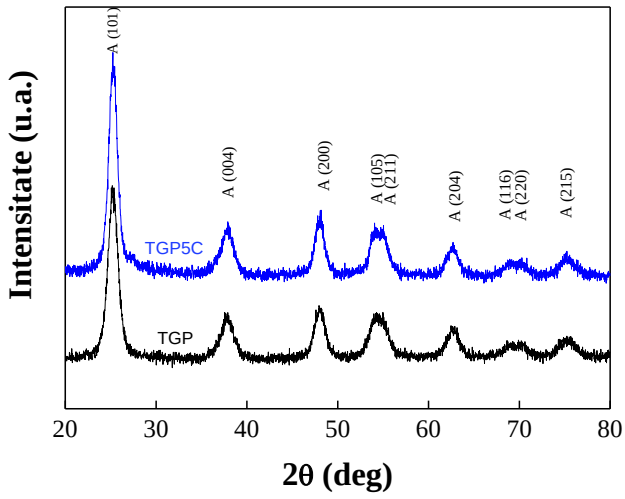

Figure 2. X-ray Diffractograms of TGP and TGP5C samples

N_2 adsorption-desorption

The adsorption-desorption isotherms of TGP and TGP5C samples are presented comparatively in Figure 3. The isotherms are of type IV with a hysteresis loop, where the desorption branch is less abrupt and the adsorption branch is more inclined. This type of isotherm corresponds to mesoporous materials with a less ordered porous structure. The pore size distribution indicated a reduction of the pore diameter after cerium introduction (5.27 nm for TGP5C compared to 5.66 nm for TGP sample). The specific surface area of both semiconductor oxides was greater than the usual values for this type of materials (116 cm^2/g for TGP5C and 141 cm^2/g for TGP sample, respectively). The decrease in pore diameter and the specific surface area for cerium-modified sample proved that cerium was deposited inside the pores of the mesoporous titania.

These superior textural properties and the crystallinity of the new synthetized photocatalysts are expected to improve the efficiency of organic products degradation.

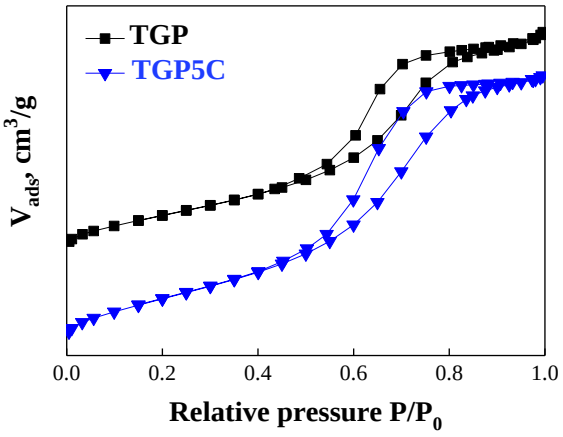

Figure 3. Nitrogen adsorption-desorption isotherms of TGP and TGP5C samples

Scanning Electron Microscopy (SEM)

Information on the mesoporous structure of the obtained oxides was confirmed by SEM microscopy (Figure 4). SEM images indicate a spherical morphology of nanoparticle aggregates, typical of mesoporous structure.

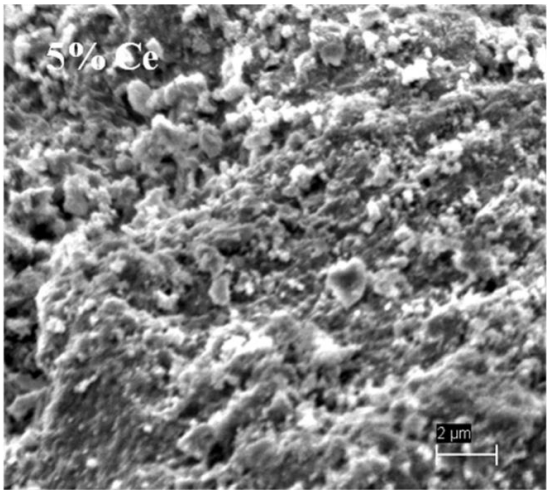

Figure 4. The SEM image of the TGP5C sample

UV-Vis spectra

The UV-Vis spectrum of TGP sample (Figure 5) indicates an ultraviolet absorption band (λ = 250 -350 nm). The strong absorption at ~250 nm is attributed to the ligand to metal charge transfer from O^{2-} to Ti^{4+} in tetrahedral geometry. A broad shoulder at ~290 nm indicates the presence of a fraction of Ti^{4+} in octahedral coordination. The peak near 330 nm suggests that TiO_2 bulk is formed in this sample. The cerium modification (TGP5C sample) leads to the absorption band expanding to the visible region (λ = 400-500 nm). These results are consistent with those presented in the literature [7] and could be attributed to the photosensitizing effect of Ce^{3+}. It was proved that the electronic transitions from oxygen to cerium require higher energy for tetra-coordinated Ce^{4+} than for hexa-coordinated Ce^{4+}. Therefore, the absorption band near 300 nm is probably due to the Ce^{4+} cations present almost with tetra-coordination.

The band gap energy of these samples has been calculated by using the equation $(\alpha h\nu)^n = k(h\nu - E_g)$, where α is the absorption coefficient, k is the parameter that related to the effective masses associated with the valence and conduction bands, n is 1/2 for a direct transition, $h\nu$ is the absorption energy and E_g is the band gap energy [5]. The Tauc plot of $(\alpha h\nu)^{1/2}$ versus $h\nu$, gives the extrapolated intercept corresponding to the E_g value. There was a decrease of the band gap after cerium introduction (2.19 eV for TGP5C sample in comparison

with 3.01 eV for TGP sample) that was favorable for activation with the visible light of the cerium modified photocatalyst.

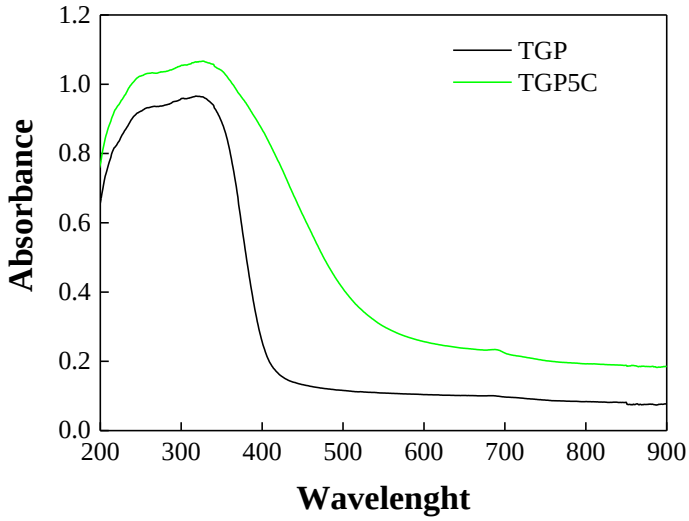

Figure 5. UV-Vis Spectra of TGP and TGP5C samples

3.2. Photoelectrochemical characterization

The photoactivity of the TGP and TGP5C samples was estimated by measuring the current density in dark and under irradiation. The dependence of the current density as a function of measured electrode potential vs. Ag/AgCl for the two tested photoactive materials is presented in Figure 6. Both for the Ce doped titania and the mesoporous titania samples, the current started to generate at -0.95 V and was increased toward the anodic direction indicating a behavior of *n*-type semiconductor. After illumination, the analyzed photoanodes showed displacements of these potentials towards more negative values, which is beneficial for the oxidation of organic compounds. Also, photocurrents increased for both samples, demonstrating their semiconductor comportment (Table 1).

Table 1. Characteristic values of current-potential curves for the TGP and TGP5C samples

Sample	Activation potential (V vs Ag/AgCl)		Current density at -0,2V (mA/cm²)	
	dark	illumination	dark	illumination
TGP	-0.97	-0.97	0.075	0.147
TGP5C	-0.75	-0.96	0.094	0.178

Samples were also analyzed by electrochemical impedance spectroscopy (EIS) to evaluate load transfer resistance (Rct) that reflects the transport of electrons and holes, as well as the transport of ions to photoanod, which is appreciated by the semi-circle in the low frequency region.

EIS measurements are presented in the form of Nyquist plots (Figure 7).

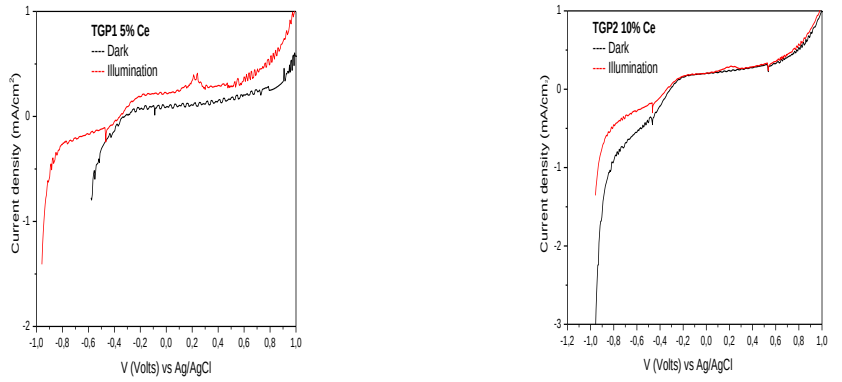

(a) (b)

Figure 6. Current-potential curves for: (a) TGP5C and (b) TGP samples

Figure 7. Nyquist plots for the TGP and TGP5C samples

As shown, the diameter of the semicircle was decreased for the TGP sample under illumination, due to a decrease of the charge transfer resistance across the electrode/electrolyte interface which was confirmed by better current-voltage characteristics of the electrode prepared with this sample.

The photo electrochemical behavior of the photo anodes constructed based on TGP and TGP5C mesoporous oxides was also investigated. The short-circuit current-time plot (J_{sc}-t), open-circuit voltage-time plot (V_{OC}-t) and photocurrent-voltage characteristics were tested both under illumination and without illumination in two electrolytes (0.2 M Na_2SO_4 and 0.2M Na_2SO_4+0.2M CH_3COOH) in a photoelectrochemical cell (Figure 1). The results are presented in Table 2.

Table 2. Photo electrochemical characterization of the photoanodes based on un-doped and Ce doped TiO_2

Electrode	Activation potential (-) Na_2SO_4		Activation potential (-) Na_2SO_4 +CH_3COOH		J(A/cm^2) X10^{-3} Na_2SO_4		J(A/cm^2) X10^{-3} Na_2SO_4+ CH_3COOH	
	illum	dark	illum	dark	illum	dark	illum	dark
TGP	1,09	0,90	1,20	1,13	0,50	0,4	2,3	1,4
TGP5C	0,40	0,30	0,89	0,80	0,02	0,01	0,20	0,10

For the photo anodes modified with TGP and TGP5C samples the activation potential under illumination was at more negative values then without illumination. Furthermore, the current density was greater under illumination proving the semiconductor comportment of both electrodes. The best results were obtained for the electrode modified of TGP sample in Na_2SO_4+CH_3COOH as electrolyte.

Table 3. The current-voltage characteristics of the presented PFC

Anode	Jsc (μA/cm^2)	V_{oc} (V)	JV_{max} (W/cm^2)
TGP	500	0,95	300 x10^{-6}
TGP5C	9	0,55	1,107x10^{-6}

The electrical performances of the photo fuel cell constructed with these photoanodes are presented in Table 3. The value of J_{SC} and JV_{max} are comparable with literature data for the same type of materials [8,9,10]. Interesting is that the best results were obtained for the un-doped mesoporous TiO_2. For the Ce-doped sample, probably the Ce^{3+} ions act as an electron trap and the current density in the external circuit is lower. However, this property was proved to be beneficial for the phenol degradation under visible light irradiation (see 3.3. Photocatalytic activity).

3.3. Photocatalytic activity

Photocatalytic oxidation of phenol in aqueous media was selected as a model reaction in order to study the catalytic efficiency of TGP and TGP5C samples, both as powders and as electrodes. The phenol degradation results are shown in Figure 8. The best results were obtained for the electrode samples in comparison with the powder ones due to a better exposure of the photocatalytically active centers to the light irradiation and a larger contact surface area with the liquid medium. The maximum photodegradation of phenol was 45.1% for the electrode prepared with the TGP5C sample. The electrode prepared with TGP sample presented 29.8% phenol degradation. The 5% cerium-modified TiO_2 sample was a more efficient catalyst than unmodified TiO_2. The introduction of Ce in the TiO_2 synthesis was beneficial for photocatalytic activity by increasing the visible absorption of TiO_2 due to its band gap narrowing. The Ce^{4+} ions, as Lewis acid, had strong capability of trapping electrons, being beneficial to the separation of electron-hole pairs [11] and, therefore, improved the photocatalytic activity. Due to the additional oxygen present on the surface of Ce-containing samples, the photoinduced electron can combine them to yield superoxide free radical with high oxidation capability [12].

It has been shown that the phenol degradation under irradiation with visible light is slower than under UV light [5]. Since the experiments were carried out only for 30 min. in order to compare the photocatalytic properties of the two materials, it is expected that at longer irradiation times the phenol degradation to be more advanced.

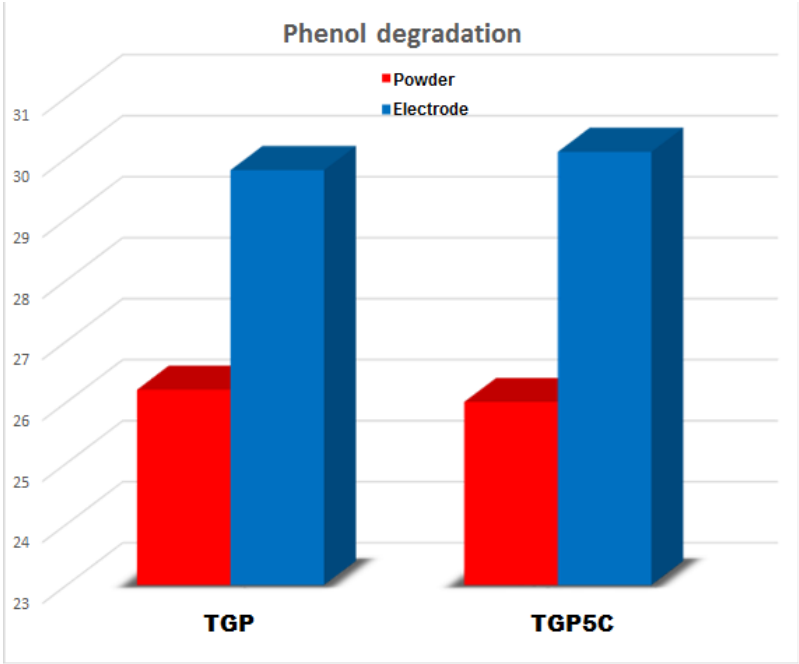

Figure 8. Variation of photodegradation efficiency of phenol for powders and electrodes

4. CONCLUSIONS

New photoactive semiconductor oxide based on mesoporous TiO_2 prepared by the sol-gel process and modified with 5% Ce by direct synthesis have been obtained and deposited thereafter by the spin coating technique onto FTO glass.

The textural and structural characterization of these materials supported their high crystallinity and mesoporous structure. Both the presence of the TiO_2 anatase crystalline phase and the high surface area were proved to be beneficial for electric current generation when the materials were tested as photoanodes in a photoelectrochemical fuel cell.

Furthermore, by cerium introduction as CeO_2 on the surface of the mesoporous TiO_2 the phenol degradation efficiency was enhanced under Vis light irradiation. Based on the obtained results, this new photoanodes could be considered for the construction of an efficient photo electrochemical system.

Acknowledgments:

The authors are grateful for the financial support from the Romanian National Authority for Scientific Research, CNCS-UEFISCDI projects number PN-III-P2-2.1-PED-2016-0473) and number PN-III-P2-2.1-PED-2016-0676, within PNCDI III.

References

[1] Yan Liu, Lihong Tian, Xinyu Tan, Xin Li, Xiaobo Chen,Synthesis, properties, and applications of black titanium dioxide nanomaterials,Science Bulletin 62 (2017) 431-441.

[2] Stavroula Sfaelou, Panagiotis Lianos, Photoactivated Fuel Cells (PhotoFuelCells). An alternative source of renewable energy with environmental benefits, Materials Science, 3(1) (2016): 270-288.

[3] Recent progress and perspectives in the photocatalytic CO2 reduction of Ti-oxide-based nanomaterials, Youngku Sohn, Weixin Huang, Fariborz Taghipour, Applied Surface Science 396 (2017) 1696–1711.

[4] Sutasinee Kityakarn, Yingyot Pooarporn, Prayoon Songsiriritthigul, Attera Worayingyong, Simone Robl, André M. Braun, Michael Wörner, (Photo)Electrochemical characterization of nanoporous TiO2 and Ce-doped TiO2 sol–gel film electrodes, Electrochimica Acta, 83 (2012) 113-124.

[5] M. Mureseanu, V. Parvulescu, T. Radu, M. Filip, G. Carja, Mesoporous CeTiSiMCM-48 as novel photocatalyst for degradation of organic compounds, J. Alloys Compd. 648 (2015) 864-873.

[6] E.K. Goharshadi, S. Samiee, P. Nancarrow, Fabrication of cerium oxide nanoparticles: Characterization and optical properties, J. Colloid Interface Sci. 356 (2011) 473-480.

[7] Jun Fang, Xinzhen Bi, Dejun Si, Zhiquan Jiang, Weixin Huang, Spectroscopic studies of interfacial structures of CeO2–TiO2 mixed oxides, Applied Surface Science 253 (2007) 8952–8961.

[8] Yao Yao, Nan Zhao, Ji-jun Feng, Ming-ming Yao, Fang Li, Photocatalytic activities of Ce or Co doped nanocrystalline TiO2–SiO2 composite films, Ceramics International 39 (2013) 4735–4738.

[9] C. Belver, J. Bedia, M.A. Álvarez-Montero, J.J. Rodriguez, Solar photocatalytic purification of water with Ce-doped TiO2/clay heterostructures, Catalysis Today 266 (2016) 36–45.

[10] J. Bharatvaj, V. Preethi, S. Kanmani, Hydrogen production from sulphide wastewater using Ce^{3+}-TiO_2 photocatalysis, Internationol journal of hydrogen energy 43 (2018) 3935-3945.

[11] Z.I. Liu, B. Guo, H. Liang, H.X. Jiang, Preparation and characterization of cerium oxide doped TiO_2 nanoparticles, J. Phys. Chem. Sol. 66(2005) 161–167.

[12] V. Augugliaro, L. Palmisano, A. Sclafani, C. Minero, E. Pelizzetti, Photocatalytic degradation of phenol in aqueous titanium dioxide dispersions, Toxicol. Environ. Chem. 16 (1988) 89–109.